Spectral Analysis and Calibration of Meteor Shower Events

Salvatore Vicinanza

Technische Universiteit Delft
Faculty of Aerospace Engineering
MSc Thesis

In collaboration with ESA/ESTEC

Spectral Analysis and Calibration of Meteor Shower Events

by

Salvatore Vicinanza

to obtain the degree of Master of Science
at the Delft University of Technology,
to be defended publicly on Wednesday October 27, 2021 at 09:30AM.

Student number:	5007437	
Project duration:	February 15, 2021 – October 13, 2021	
Thesis committee:	Dr. D. M. Stam,	TU Delft, chair
	Dr. ir. W. van der Wal,	TU Delft, responsible thesis supervisor
	Mr. J. Zender,	ESA/ESTEC, company supervisor
	Dr. R. Rudawska,	ESA/ESTEC, company supervisor
	Dr. A. Menicucci,	TU Delft, examiner

An electronic version of this thesis is available at http://repository.tudelft.nl/.

TU Delft

Preface

This report outlines the work done within the project "Spectral Analysis and Calibration of Meteor Shower Events", a collaboration between the European Space Agency's Meteor Research Group and Delft University of Technology. The project had a net duration of around seven months, excluding the Literature Study, and is used by the author as part of the thesis module within the M.Sc. Aerospace Engineering programme offered by Delft University of Technology.

Readers with a particular interest in the fields of meteor spectroscopy and atmospheric studies would hereafter find an innovative approach for the elevation-dependent atmospheric calibration of meteor spectra observed from optical ground-based cameras. Moreover, readers would discover interesting aspects about the influence which different meteoroid-atmospheric interactions have on meteoroid composition inferences.

I would like to express special thanks to the Meteor Research Group, whose members have kindly welcomed me on-board.
In particular, my immense gratitude goes to my supervisors, Joe Zender and Dr. Regina Rudawska:
Thank you for having shared your exceptional knowledge, experience and passion with me,
and for being understanding and patient guides, who never spared words of appreciation.

My most sincere appreciation goes to my supervisor at Delft University of Technology, Dr.ir. Wouter van der Wal:
Thank you for supporting this collaborative project with great enthusiasm, always available to provide valuable advice.
Your help and cordiality have really boosted and motivated my work for the best.

Moreover, I would like to thank Dr. Detlef Koschny, for his involvement and help.
Thanks for always taking the time to answer a question or initiate a fruitful discussion.

Last but not least, I would like to thank Dr. Daphne Stam, for her openness to dialogue and precious suggestions.
Without her specialised knowledge, the outcome of this project would have not been the same.

Salvatore Vicinanza
Delft, October 2021

Contents

List of Symbols and Abbreviations

Abbreviation	Full name or meaning
a.u.	Arbitrary unit
CCD	Charge-Coupled Device
CILBO	Canary Island Long-Baseline Observatory
CNN	Convolutional Neural Network
CPU	Central Processing Unit
Dec	Declination
DN	Digital Number
ESA	European Space Agency
ESTEC	European Space Technology Centre
FOV	Field Of View
GUI	Graphical User Interface
ICC	Intensified CCD Camera
IMC	International Meteor Conference
km	Kilometer
LSQ	Least SQuares
LT	Local Time
m	Meter
MCMC	Markov Chain Monte Carlo
MetRec	Meteor Recognizer
ML	Machine Learning
MRG	Meteor Research Group
NIR	Near-infrared
nm	Nanometers
PAL	Phase Alternate Line
PARADE	PlasmA RAdiation DatabasE
px	Pixel
RA	Right Ascension
s	Second
SI	International system of units
s.l.	Sea level
SNR	Signal-to-Noise Ratio
STIS	Space Telescope Imaging Spectrograph
TAPAS	Transmissions of the AtmosPhere for AStromomical data
UT	Universal Time
UV	Ultraviolet
UVA	Ultraviolet A
WCS	World Coordinate System

Introduction to the Paper

After the disintegration of asteroids and comets in space, "children" products, i.e. meteoroids and interplanetary dust (Borovička et al., 2005), are generated and continue moving around space, generally along the orbit of their "parent" body. The *meteoroids* are the biggest products of this disintegration, with size ranging between 30 micrometers to 1 m according to Koschny and Borovicka (2017). When the orbit of these bodies encounters the Earth, they collide with the Earth's atmosphere. The interaction of meteoroids with the atmosphere heats the bodies to incandescence, resulting in luminous streaks in the sky, visible from ground: the *meteors*. The heating of space bodies in the atmosphere is a result of a process called meteor ablation. During meteor ablation, the aerodynamic pressure acting around the body exceeds the body's material strength, causing the body to loose mass and eventually break-up. Meteor ablation acts as filter, letting only high-density meteoroids to pass through and reach ground without completely degrading Gritsevich and Koschny (2011). The bodies which survive their passage in the atmosphere and can be found on Earth's surface are known as *meteorites*. According to Jenniskens et al. (2004), only below 8% of meteoroids in the size range of 10 mm to 50 mm detected by meteor observations reach ground as meteorites. The left plot in fig. 1 visualises the different definitions of meteoroid, meteor and meteorite. Meteors with absolute brightness higher than -4 are referred to as *fireballs* (Koschny and Borovicka, 2017).

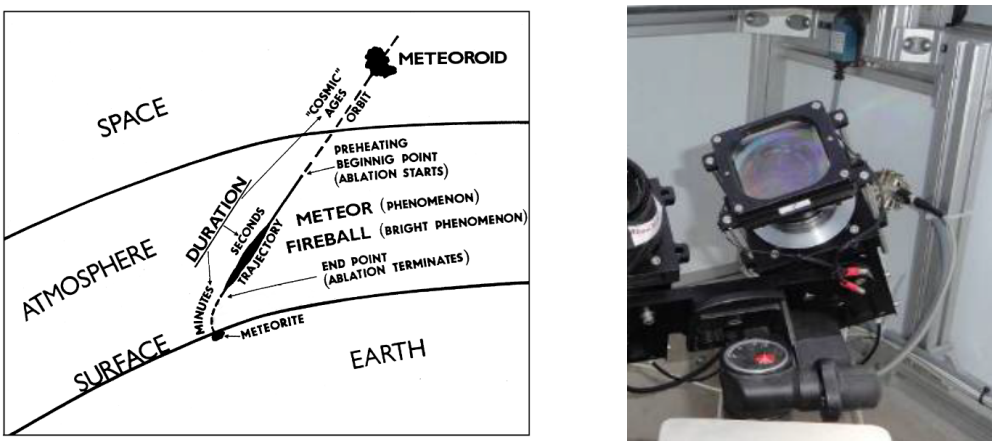

FIGURE 1: *Left*: Illustration of the progression of a *meteoroid* into a *meteor*, after the space body collides with the Earth's atmosphere, and *meteorite*, after the body reaches the surface (Ceplecha et al., 1998). *Right*: Photography of the optical video camera in CILBO observatory, in Tenerife, with a diffraction grating on top (Koschny et al., 2013).

As the meteor ablates in the atmosphere, particles belonging to the meteoroid are excited from its surface (Ceplecha et al., 1998). The collision of the space body with the atmosphere also excites atoms and molecules from the atmosphere. These particles emit photons, as their excitation during meteor ablation induces a transition between energy levels; this transition happens at a specific wavelength, obtained from the Planck's formula (Liebhart et al., 2011). The contributions of the wavelength-specific radiation generated by the emission of elements of both atmospheric and meteoric origin add together in the meteor spectrum. The most common way to observe meteor spectra for scientific purposes is to use ground-based optical cameras, mounting diffraction gratings in front of their lenses. The right image in fig. 1 shows the optical camera used in this research, with the diffraction grating on top. After the light impinges on the grating, it follows a pattern of destructive and constructive interference; the meteor spectrum results from this interference. Different orders of constructive interference happen at a unique set of angles (θ_m, in the left plot of fig. 2), specific for the setup used (Loewen and Popov, 1997). The middle image in fig. 2 gives an example of the first-order meteor spectrum observed from the ground-based camera used in this project. The right plot shows the intensity of each feature in the spectrum.

Meteor emission spectra are analysed using a technique called meteor spectroscopy, which allows to gain information about properties and chemical composition of the body generating the meteor event (Rudawska et al., 2020). The inference of chemical composition from meteor spectra is not trivial. This involves the estimation of the intensity of each line in the meteor spectrum, of the nitrogen bands and the ablation temperature. This estimation entails manual (Vojácek et al., 2019) or (semi-)automatic fitting of the observed meteor spectra (Borovička et al., 2005; Jenniskens, 2007): using an energy transfer model, a synthetic spectrum is modelled by tuning the parameters (line intensities, N_2 bands and ablation temperature) and it is compared to the spectrum of the observed meteor. The goal of the fitting is to find the right combination of parameters for the synthetic and observed spectrum to coincide. After the spectrum is fitted, the estimated parameters are interpreted to retrieve the meteoroid's composition. In this research project, the composition of meteoroids observed from optical cameras on ground is inferred through Bayesian inference, explained in appendix G.

FIGURE 2: *Left*: Schematic of a transmission grating which lets the first-order spectrum through. *Middle*: Event 01-06-2012, 22:51:00; zeroth-order meteor (left of the image) and its first-order spectrum (right of the image) seen from CILBO observatory, in Tenerife. *Right*: Intensity of the first-order spectrum in digital numbers, after the spectrum was retrieved from the total image in the *middle*.

Meteor spectroscopy is of great scientific relevance as discoveries about parent bodies' compositions support numerous areas of scientific research. Studies about the Solar System evolution, for example, rely on the knowledge of asteroids' and comets' chemical properties, as these carry information about Solar System's history (Borovička et al., 2005). Moreover, meteor studies are relevant in the field of astrobiology. As underlined by Silber et al. (2018), these studies are helpful in determining the composition of meteoroids which may have carried to Earth the chemicals that fostered life in the early days. Planetary defense strategies also heavily rely on discoveries and information about interplanetary material reaching our planet. Impacts from meteoroids are a hazard to daily space activities: they disturb the operations of Earth-orbiting satellites and modify the atmospheric composition through emissions (Cander, 2019). In that context, forecasting of meteoroids' collisions to Earth is paramount to establish effective mitigation actions to these threats. However, as discussed by Vaubaillon et al. (2015), forecasting is reliable as long as the body's parent body is known. In this context, meteor spectroscopy plays a supporting role to planetary defense studies: thanks to its ability to characterise the composition of meteoroids impacting the Earth, it supports the knowledge about meteoroids' orbits and formation coming from dynamics studies, thus allowing to enhance knowledge about parent bodies. Finally, research on space resource exploitation (e.g. asteroid mining) profits from better comprehension of the structural characteristics and composition of space bodies.

Past meteor spectroscopy research on optical systems' observations revealed that three elements of meteoric origin are most commonly distinguished in meteor spectra: Fe, Mg and Na (Trigo-Rodríguez et al., 2004). Although the relative spectral abundance of these three atoms varies for each event, the existence of trends in spectral behaviors of different meteors makes it possible to classify the different meteor spectra into few classes with distinctive composition features. Borovička et al. (2005) established a general meteor spectra classification convention, widely adopted by scholars in this area. Based on this, four main meteor spectra classes are distinguished: (1) *Na-free*, (2) *Na-rich*, (3) *Irons*, respectively populated by spectra with a distinctive depletion of sodium, enrichment in sodium and dominance in iron, compared to (4) *Mainstream* meteors, which have relative elemental abundances close to the chondritic composition[1]. The meteor classes identified through this classification include both *shower meteors* and *sporadic meteors*: the former are bodies belonging to a recognized meteoroid stream and with a known parent body (e.g. Geminids with parent comet 3200 Phaeton), while the latter are not associated to any definite parent body. The researchers observed that shower meteors generated from the same parent body generally belong to the same spectral class. This might suggest that the commonality of spectral features among meteors within the same class reflects the similarity in the parent body's chemical composition, to a large extent. Nonetheless, there are cases of remarkable difference in the spectral appearances of meteoroids from the same stream.

One of the greatest shortcomings of meteor spectroscopy is that it is based on the study of *remote* observations; the meteor spectra observed from ground are not the direct reflection of the meteoroid composition, as their appearance is affected by various other factors, here called *external factors*. The Earth's atmospheric extinction, different meteoroid entry conditions (e.g. meteoroid speed and its ablation height), the time of meteor observation and instrumental errors (e.g. camera spectral sensitivity) are all external factors, and influence the intensities of meteor spectral features as described in the following paper. These factors could be one reason behind the differences in the spectral appearances of meteoroids from the same stream. The other could be a difference in composition among the meteoroids. The problem is that one cannot distinguish between the spectral features induced by the meteoroid composition and those due to effects from external factors, if the influence of these factors is not well known. The lack of knowledge about the influence of external factors on remote observations of meteors affects the quality of meteoroid composition inference from their spectra. This research's objective is to improve the quality of meteoroid composition inference from meteor spectra, by assessing the

[1] Chondritic composition is characteristic of *chondrites*, primitive bodies containing distinct morphological inclusions called chondrules (Jenniskens, 2007). Chondrites are bodies which never melted and had very few interactions since their formation, thus can reveal early Solar System conditions.

degree to which these external factors influence the appearance of meteor spectra, and by improving the calibration pipelines used to correct meteor spectra for external factors' influence.

Draft Paper

Spectral Analysis and Calibration of Meteor Shower Events

SALVATORE VICINANZA

Faculty of Aerospace Engineering, Delft University of Technology, Delft, The Netherlands
Email: S.Vicinanza@student.tudelft.nl

ABSTRACT

By analysing the spectra of meteors ablating in the Earth's atmosphere, one can acquire valuable information about the composition of their parent bodies (asteroids and comets). A challenge to the accurate composition inference comes from external factors: factors other than the parent body composition, which affect the meteoroid-atmosphere interaction and hence influence the appearance of meteor spectra. External factors of interest in this study are variability of atmospheric extinction with elevation, changes in meteoroid entry speeds, ablation conditions and temporal evolution of meteoroids' interaction in space. The goals of this research are to assess to what degree these external factors influence the appearance of meteor spectra and meteoroids' composition retrieval from them, and to improve the calibration pipelines used to correct meteor spectra for external factors' influence.

The research was done within the framework of ESA's Meteor Research Group (MRG) and used as main data source the ground-based observations collected from optical cameras in CILBO observatory. First, the MRG calibration pipeline implemented by Zender et al. (2014); Rudawska et al. (2020) was improved — an automatic routine was developed to perform elevation-dependent atmospheric correction of meteor spectra. The new correction was based on the extinction law by Appenzeller (2012), adjusted to account for the variation of atmospheric extinction as meteoroids' elevation changes during their path in the atmosphere. A statistically significant improvement resulted on the calibration pipeline: the intensity of spectral features below 400nm increased by more than 20% when the elevation dependence of the extinction was considered as part of the atmospheric correction.
The MRG procedure for spectral analysis was modified. This allowed to analyse meteor spectral features emitted over a wavelength range of 350-840 nm; originally the MRG analysed only the 400-800 nm spectra and hence missed emission features, especially in the UVA. In this new spectral analysis, intensities of meteor spectral features and elemental abundances were inferred from the calibrated observed spectra through a semi-automatic spectral fitting which used an optically thin radiative transfer model. The resulting spectral features were then correlated to external factors observations: meteoroid entry speeds, ablation conditions and year of meteor observation.
The external factors' analysis performed on our set of 198 low-speed (<20 km/s) *total* meteor spectra revealed a strong correlation between meteoroids' entry speed and the number density of elements — number densities of Na and Fe (meteoric elements) decreased at a rate of -10 and $-3\,(\mathrm{m/s})^{-1}$ with speed, while O and N (atmospheric elements) increased at rate of $16\,(\mathrm{m/s})^{-1}$. Moreover, the study conducted on *individual frames*' spectra concluded that variations of line intensities over frames are correlated with changes in the ablation temperature with height. Finally, changes in meteoroid composition were seen among meteors generated from the same showers (Geminid and Antihelion Source) but observed in different years, possibly due to different meteoroid stream filaments observed.

Keywords: shower meteors, spectroscopy, meteoroid composition, entry speeds, atmospheric extinction.

1. INTRODUCTION

Meteor spectroscopy is based on remote observations of ablating meteoroids in the atmosphere. For this reason, although meteor spectra collected by on-ground equipment reflect the internal composition of the meteoroid, they are also affected by the type of meteoroid-atmosphere interaction taking place during each event. Different factors, other than the meteoroid's internal composition, influence this interaction. These are called *external factors* and include meteoroid entry speed, atmospheric extinction, ablation conditions and stream formation age.

Research from Vojácek et al. (2019), Matlovič et al. (2020) and Rudawska et al. (2020) noted that the speed of the meteoroid at the moment of its entry in the atmosphere, has a strong influence on spectra. They observed that this factor directly relates to meteor ablation: during slow entries, the ablation temperatures reached are so low that only highly volatile elements (e.g. Na) are sufficiently excited to evaporate. According to the experimental simulations on meteorites by Matlovič et al. (2020),

Na-rich spectra appear in cases of very slow bodies irrespective of the meteoroid's actual composition. In most cases, this means that the intensities of Na lines, relative to line intensities of more refractory elements like Mg, do not reflect the effective dominance of sodium in the meteoroid's composition; by contrast, this is only the consequence of the body's specific conditions of ablation, which do not favor refractory elements' emission.

The Earth's atmosphere influences the amount of light transmitted from the meteor to the observing camera. Consequently, it modifies the intensities of meteor spectra features observed from ground. To accurately infer the composition of meteoroids in space, it is thus important to correct for the effects of optical atmospheric extinction. Atmospheric extinction varies with elevation of the target body; specifically, it varies with its angular term (angle above horizon) and linear term (elevation above ground). Therefore, a precise calibration pipeline should provide a dedicated correction based on the meteor's elevation change along its path in the atmosphere. Instead, in meteor spectroscopy, generally the same atmospheric correction is applied over all the frames observed for a meteor event, using a "standard curve" of extinction per event (Dubs and Maeda, 2016); calibrations with these standard curves do not account for the variation in atmospheric extinction along the meteor's path.

Furthermore, spectral observations of meteors along their paths in the atmosphere are affected by the diverse ablation conditions found at the different heights, particularly the ablation temperature and pressure. However, most studies like Jenniskens (2007) and Rudawska et al. (2020) perform analyses on the integrated (or total) spectra, where the line intensities result from the average of the pixel intensities along the whole meteor's path; integrating the spectrum allows to decrease the noise in spectra, but the variability per height of the spectrum is averaged together, thus lost. By contrast, studying the change in meteoric elements emissions with height can reveal how strong is their correlation with changes in ablation temperatures and pressures with height. The spectral evolution with height was investigated by Borovička et al. (1999); however, the research focused only on the Na depletion in 1998 Leonid meteors and did not investigate in detail its correlation with changes in ablation conditions.

From Borovička et al. (2005) and Vojácek et al. (2015), we learn that the spectra of meteors belonging to the Geminid shower have significant variation in Na content. The explanation was linked to the age of formation of the observed meteoroids: the Geminid stream was probably formed in different ages and its older meteoroids have lower Na content due to the longer exposure to radiation in space. However, the age of meteoroid formation is expected to influence the content of all meteoric elements, and not only Na; yet, this investigation was not done on other meteoric elements. Moreover, one can assume that younger and older meteoroids move along different orbits, and may impact the Earth at different times; however, past researchers did not correlate the variations of Na content to the time of meteor observation, although this could bring compelling arguments to their conclusions.

Although various studies have reported on the impact of external factors on meteoroid composition inference from meteor spectra, it is currently not possible to accurately constraint the extent to which external factors bias the inference of meteoroid composition on a large scale. In fact, past researchers could only focus on the specific factors significant for the small and unrepresentative sets of spectra analysed. The analysis was conducted on single fireball events (Borovička, 1993), meteors belonging to one unique shower (Leonids in Borovička et al. (1999) and Jenniskens (2007)), or specific classes of spectra (17 Na-enhanced spectra in Matlovič et al. (2020)). Vojácek et al. (2019, 2015) and Borovička et al. (2005) studied more representative data sets, around 100 sporadic and shower meteor spectra; however they only analysed the influence of meteoroid entry speed and structure, with minimal focus on the other external factors. Additionally, calibration pipelines available from literature are often not suited for accurate analyses of external factors on large data sets: they require substantial manual intervention and lack corrections for external factors, like the absence of atmospheric correction in Rudawska et al. (2020).

The main objective of this study is to improve the quality of meteoroid composition inference from meteor spectra and the software tools used for their analysis. We aim to do so by assessing to what degree the external factors influence the appearance of meteor spectra, and by improving the calibration pipelines used to correct meteor spectra for external factors' influence. This research addresses two main questions:

i) *How do different meteoroid-atmosphere interactions, induced by varying atmosphere and meteoroid entry conditions, reflect on meteor spectral features and affect their analysis?*
ii) *How can the calibration pipelines be improved to more accurately retrieve meteoroids' compositions from meteor spectra?*

The automation of the calibration pipeline was the first major area of improvement from this study. After section 2 introduces the process of acquisition and reduction of data selected for the successive spectral analysis, section 3 explains the advancements brought to the original calibration pipeline. In particular, section 3.1 describes the development of a fully-automated wavelength calibration pipeline, tested to work effectively for our complete set of optical first-order meteor spectra.

The second major improvement was a better understanding about the effects that atmospheric extinction variation with elevation has on meteor spectra. To do so, an elevation-dependent procedure for atmospheric calibration was developed and validated. Section 3.2 describes this procedure and the research about the significance of elevation dependence on the accuracy of atmospheric correction and meteoroid composition inference.

Third, the research analysed the relation between meteor spectra appearances and meteoroids' entry speeds — using a larger set of low-speed meteors (around 200 events) compared to what considered in past studies; then, it analysed the evolution of shower meteor spectral features over the meteor's path and in function of the observation time. This study is reported in section 4. To conclude, section 5 reports the main results and discusses their implications for meteor spectroscopy research.

2. DATA ACQUISITION AND DATA REDUCTION

This section introduces the processes of acquisition of meteor data and the reduction of the acquired data for successive spectral analyses. Section 2.1 explains the experimental setup and equipment used during this project. Then, section 2.2 and 2.3 explore the process of data reduction, from the selection of the meteor spectra used for successive spectral analyses, to the dark-current, flat-field and background correction of raw images.

2.1. Experimental Setup: CILBO

The project used as data source the visible first-order spectra and zeroth-order meteors observed at the Canary Island Long-Baseline Observatory (CILBO), operated by ESA's Meteor Research Group (MRG). CILBO has a double-station setup of intensified CCD video cameras (ICC). Three image-intensified cameras are mounted in two different locations: ICC8 and ICC7 mounted in Tenerife (CILBO-T station) and ICC9 in La Palma (CILBO-L station); all CILBO cameras monitor the same portion of sky, as sketched in fig. 3. Data from ICC8 and ICC7 represent the primary source for this project. ICC7 records the zeroth order of meteors. ICC8 is equipped with an objective grating in front of its lens (see fig. 4): it records meteors' first-order spectra. Both ICC8 and ICC7 have a frame rate of 25 frames per second (time resolution of 0.04 s), an image resolution of 768×576 px and 8 bit dynamical accuracy (Koschny et al., 2013).

ICC7 and ICC8 run on the same local computer, with ICC7 continuously recording images of the night sky and ICC8 waiting in standby — when the MetRec software (Molau, 1999) detects a meteor in ICC7's field of view (FOV), it triggers the acquisition of the frames from ICC8; then, both ICC7 and ICC8 frames with detected meteors are saved in the computer hard-disk as BMP files. The acquisition process by MetRec often associates a slight delay (order of 1/25 sec) between the zeroth-order image detection on ICC7 and the acquisition of the corresponding first-order spectra from ICC8. This delay requires a time correction in the meteor spectra calibration; specifically, a time interpolation is applied to the meteor's ICC7 pixel location, in order to obtain the meteor's position at the time when MetRec acquires the ICC8 image.

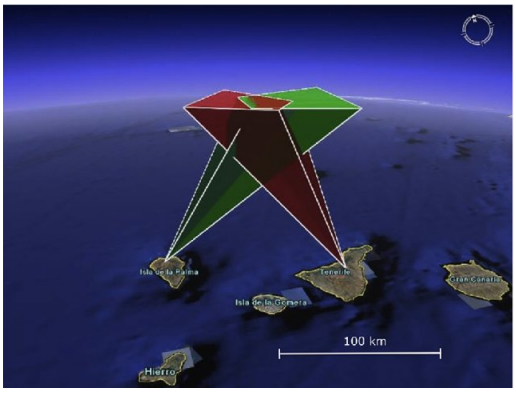

FIGURE 3: Sketch of CILBO's double station camera set-up (Koschny et al., 2013).

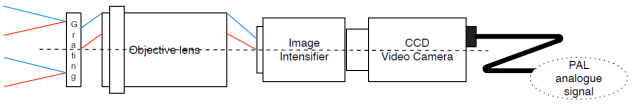

FIGURE 4: CILBO's ICC8 block diagram (Zender et al., 2014).

2.2. Selection of Meteor Events

Before being able to perform analyses on the meteor spectra, the acquired data necessitates reduction. The first step of the data reduction routine was discarding meteor events whose first-order spectra were exceedingly faint, or exceedingly bright — meteors fainter than +2.0 mag generated spectra with low signal-to-noise ratio (SNR), where element lines could be hardly distinguished from the background noise by spectral analysis tools; by contrast, meteors brighter than −1.9 mag *often* generated saturated spectra, where it was not possible to separate the spectral contribution of each individual element. Neither type of spectra permits an accurate inference of the meteor's chemical composition, which is based on the analysis of the distinctive emission patterns of all elements making up the meteor. For this reason, only events brighter than +2.0 were selected for this project. For meteors brighter than -1.9 mag, a case-by-case selection was performed to remove events with saturated spectra.

A further, manual selection was performed. This aimed at removing exceptional events — cases where meteors had brightness within the interval of interest but extremely faint first-order spectra, or spectra with hardly-distinguishable lines. A dedicated web-based Graphical User Interface (GUI) was developed to facilitate this manual selection; the GUI is described in appendix A. Exceptional events encountered while inspecting CILBO data include: cases where clouds, or secondary-order spectra of the Moon, covered part of the meteor spectrum of interest; cases with entry angle too close to the horizon (90 deg), generating spectra with horizontally overlapping and non-separable lines; cases with a too bright background, which concealed meteor spectra features.

TABLE 2: Results from the meteor events' selection within data reduction pipeline. Columns *ICC7 Events* and *ICC8 Events* give the number of events recorded by ICC7 and ICC8. Column *Matches* gives the number of events recorded simultaneously by both ICC7 and ICC8. Column *Selected* gives the number of events after meteor selection; in parenthesis, the percent ratio of the value in *Selected* and the corresponding in *Matches*.

Year	*ICC7 Events*	*ICC8 Events*	*Matches*	*Selected*
2012	11312	19492	**4127**	**91 (2.2%)**
2013	19435	10385	**667**	**110 (16.5%)**
2014	12647	4884	**195**	**39 (20.0%)**
2015	18377	25423	**5286**	**54 (1.02%)**
2016	27481	24135	**2734**	**48 (1.76%)**
2017	10388	9050	**684**	**12 (1.75%)**
2018	1150	484	**147**	**1 (0.68%)**
2019	3088	1262	**335**	**0 (0%)**
2020	0	1077	**0**	**0 (N/A)**
Total	103622	96231	**14174**	**355**

As the calibration routine requires that both zeroth-order images and first-order spectra are available, the selection was performed among the events recorded simultaneously by both ICC7 and ICC8. These events are indicated in the column *Matches* of table 2. The selection of meteor events scaled down the total set of 14174 visible meteor events, recorded from both ICC7 and ICC8 in the period 2012-2018, to a total of 355 events to use in the project. Table 2 gives information about yearly distribution of the 355 events used in the project.

2.3. Radiometric Calibration

The basic equation used for radiometric calibration is expressed below:

$$\text{RAW} = t \cdot V \cdot Q \cdot I + \text{DC} \tag{1}$$

where RAW is the pixel value of the raw image (spectra seen from CILBO), t the exposure time, I the photon flux, Q the variation in quantum efficiency, V the vignetting and DC the dark current noise. The primary goal of the dark current and flat-field correction was to remove term DC and correct term V from eq. (1). This allows to obtain a calibrated image expressed as in the following:

$$\text{Calibrated Image} = \frac{\text{RAW} - \text{DC}}{\text{Flatfield} - \text{DC}} \tag{2}$$

The dark current and flat-field correction is schematised in fig. 5 and is important to remove artifacts in the image which affect the appearance of spectra: flat-field correction removes the effects of illumination variations in the optical system, like vignetting and distortions in the optical path; dark current correction removes the effects of electrons which flow in the detector, even when there is no light incident on it. To perform dark current and flat-field correction on the selected meteor spectra ("RAW" in eq. (2)), ICC8 calibration exposures must be provided, i.e. the dark current (I) and flat-field exposures (II), referred as "Flatfield" and "DC" in eq. (2). The major assumption considered here was that the calibration exposures do not have significant change in the time period 2012-2018, hence could be used for the radiometric calibration of all meteor events recorded in that period.

The dark current calibration exposure (I) is obtained by taking the median of three zero-integration images of ICC8. These were images taken on date 01/01/2010, when the camera was covered by the lid — they give the signal on the photodetector when no light is incident on it.

The flat-field calibration exposure (II) is obtained starting from ICC8 recording on date 17/05/2012 at 00:00:00, when the detector was uniformly illuminated by the bright sky. After correcting this image for the dark current exposure ("DC"), a Gaussian blur is applied to mimic background light distribution and remove outliers. The image is then normalised for its peak value. Finally, a uniform filter is applied, which replaces each pixel's value by the mean of an area centred in the pixel and having area $4\times4\,\text{px}^2$; this is useful to further reduce noise in the image. The resulting image, after blurring, normalisation and noise reduction, is the calibration exposure used for the flat-field correction ("Flatfield" in eq. (2)).

The background subtraction is the last step of data reduction. The background image is computed from the median of the first and last three frames recorded per each event. These six frames record the sky right before and after the meteor passage was detected on ICC7; they do not have a meteor visible on them, thus are of no use for the spectral analysis, but they are useful for calculating the background image. The background image is subtracted from ICC8 frames, after those have been corrected for the dark current and flat fielding. The results are so-called subtracted images, which are the inputs for the calibration described in section 3. Finally, the astrometry calibration is computed through an external tool called Astrometry.net; the procedure is described in appendix B, as it is beyond the scope of this paper.

3. METEOR SPECTRA CALIBRATION

How can the calibration pipelines be improved to more accurately retrieve meteoroids' compositions from meteor spectra?

This section aims to address this research question, introduced in section 1, for each of the three major processes of the calibration pipeline on which this study concentrated: wavelength, atmospheric and sensitivity calibration. To do so, first the methodology of the calibration process is described; then, the effects of calibration errors on spectral inferences are discussed; finally, the major improvements made to the original MRG pipeline to mitigate these effects are highlighted.

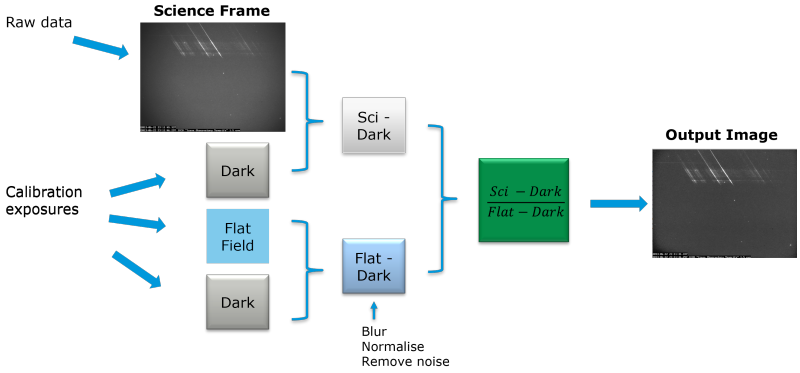

FIGURE 5: Schematic of the dark current and flat-field correction routine on CILBO's data.

3.1. Wavelength Calibration

The aim of the wavelength calibration is to associate a specific wavelength to each feature in the emission spectrum, and hence identify the chemical element to which the emission feature belongs.

3.1.1. Methodology: Reference frame transformations

The new wavelength calibration process developed during this study is based on the procedure explained by Zender et al. (2014): starting from the celestial coordinates of a zeroth-order meteor observed on ICC7 (RA_0 and Dec_0), the position on the ICC8 image of each feature of the first-order spectrum (x_λ and y_λ, with λ being the wavelength at which the feature appears) is determined by applying six steps, involving coordinate frame transformations. Theoretically, the procedure is the same as the one used in the original MRG calibration pipeline. However, since it had been wrongly implemented in the past, a new implementation of this pipeline was realised within this new research. The six steps of the wavelength calibration process are described below and summarized in schematic boxes.

(I) Retrieve the position of the meteor's zeroth order on ICC7 image (x_0,y_0). This is calculated by MetRec at the moment of the meteor observation and passed in the form of an information (.INF) file.

$$\boxed{\text{ICC7 Image} \xrightarrow{\text{.INF file}} (x_0, y_0)}$$

(II) Transform the position of the meteor's zeroth order on ICC7 into its celestial coordinates (RA_0 and Dec_0), using ICC7 World Coordinate System (WCS) obtained from astrometry calibration (see appendix B).

$$\boxed{(x_0, y_0) \xrightarrow{\text{ICC7 WCS}} (RA_0, Dec_0)}$$

(III) Convert the meteor's position from a celestial frame to a local-horizontal frame ($\mathbf{x}_0^{loc\_hor}$) centered at CILBO's ICC7/ICC8 station (CILBO-T). Information about latitude, longitude and height of the CILBO-T station was provided by Koschny et al. (2013).

$$\boxed{(RA_0, Dec_0) \xrightarrow{\text{CILBO-T lat, lon, h}} \mathbf{x}_0^{loc\_hor}}$$

(IV) Convert the zeroth-order meteor's position from the local-horizontal frame to the ICC8 grating-centred frame ($\mathbf{x}_0^{grat}$). Knowing the azimuth (α), elevation (ϵ), tilt angle (γ)[1] and bore-sight angle (β)[2] of the grating, the Euler rotation matrices (R_x, R_y, R_z) are used for the transformation, as shown in eq. (3) below:

$$\mathbf{x}_0^{grat} = R_z(\alpha) R_y(\epsilon) R_z(\gamma) R_x(\beta) \cdot \mathbf{x}_0^{loc\_hor} \tag{3}$$

$$R_x(\beta) = \begin{bmatrix} 1 & 0 & 0 \\ 0 & \cos(\beta) & -\sin(\beta) \\ 0 & \sin(\beta) & \cos(\beta) \end{bmatrix} \tag{4}$$

where eq. (4) shows R_x used for the rotation around x of the bore-sight angle β, provided as example.

$$\boxed{\mathbf{x}_0^{loc\_hor} \xrightarrow{R_{x,y,z}(\alpha,\epsilon,\gamma,\beta)} \mathbf{x}_0^{grat}}$$

(V) Calculate the coordinates in the grating-centred frame of each feature of the ICC8 first-order spectrum, i.e. $\mathbf{x}_\lambda^{grat}$. The x-, y- and z-axis terms of the first-order vector $\mathbf{x}_\lambda^{grat}$ (A', B' and C') are obtained starting from the x-, y- and z-axis terms of the zeroth-order vector $\mathbf{x}_0^{grat}$ (A, B and C), as defined below:

$$\begin{aligned} A' &= -A + md\lambda \\ B' &= -B \\ C' &= -\sqrt{(1 - A'^2 - B'^2)} \end{aligned} \tag{5}$$

Figure 6 visualises the 3D transformation defined in eq. (5). The first term of the 3D transformation is based on the grating equation:

$$\sin\theta_m = md\lambda \tag{6}$$

The minus sign on the second term of eq. (5), B', indicates that, while the coordinates of the meteor are on the negative side of the coordinate frame, the spectrum is projected on the positive one (see fig. 6). The last term (C') transforms $\mathbf{x}_\lambda^{grat}$ into a unit vector.

[1] Tilt angle: rotation of the x,y-plane of the grating around its z-axis
[2] Bore-sight angle: grating rotation around its x-axis.

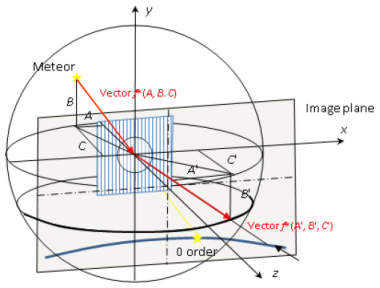

FIGURE 6: Vector components of incident and diffracted ray, and Cartesian coordinate system orientation (Dubs and Maeda, 2016).

$$\mathbf{x}_0^{grat} \xrightarrow{\text{grating eq.}} \left(\mathbf{x}_{\lambda,1}^{grat}, \mathbf{x}_{\lambda,2}^{grat}, ..., \mathbf{x}_{\lambda,n}^{grat}\right)$$

(VI) Calculate the position of each feature of ICC8 first-order spectrum (x_λ, y_λ). To do so, first the grating-centred coordinates of the features in the spectrum are converted into corresponding coordinates in the Earth-centred celestial frame (RA_λ, Dec_λ); then, the celestial coordinates are converted into ICC8 pixel locations, using ICC8 WCS (appendix B).

$$\mathbf{x}_\lambda^{grat} \xrightarrow[\text{CILBO-T lat, lon, h}]{\text{grat. eq., } R_{x,y,z}(\alpha,\epsilon,\gamma,\beta)} (RA_\lambda, Dec_\lambda) \xrightarrow{\text{ICC8 WCS}} (x_\lambda, y_\lambda, \lambda)$$

3.1.2. *Wavelength errors: Causes, distribution and effects*

The pipeline described in section 3.1.1 allowed to perform an automatic wavelength calibration on all the meteor spectra selected during data reduction. At the end of this process, wavelength-calibrated spectral profiles were obtained, similar to those shown in fig. 7. However, as seen from the bottom figure of fig. 7, the automatic wavelength calibration did not always provide accurate results. For this reason, we investigated the wavelength errors, to understand their causes, distribution and effects on meteoroid composition inference. An automatic routine was developed for the estimation of the wavelength errors, described in appendix C. The wavelength error estimation was based on the comparison of reference emission lines, i.e. lines of Mg, Na and O with known emission spectrum, to lines in the observed meteor spectrum.

Causes. After having estimated the wavelength errors for the selected 355 events, various possible sources of error were considered and carefully analysed during this study:

(i) Inaccuracy of astrometric calibration (errors in WCS);
(ii) Uncertainty in information about the position of the zeroth-order meteor, provided by MetRec.
(iii) Inaccuracy in the value of the bore-sight angle (β);
(iv) Errors in the ICC7/ICC8 time interpolation;
(v) Inaccuracy in the mathematical equations.

To understand which of these sources had greatest influence on the errors observed, several tests were

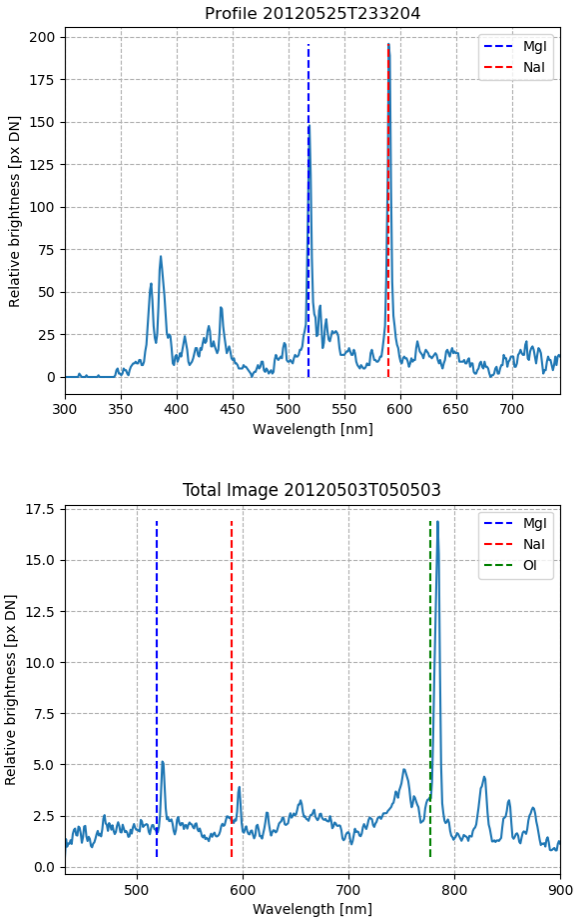

FIGURE 7: Example of spectral profiles obtained at the end of the wavelength calibration process. *Top*: Event 25/05/2012 23:32:04, no wavelength error. *Bottom*: Event 04/05/2012 05:05:03, wavelength error of 6.9 nm

conducted. The results from the tests concluded that the dominant source of wavelength error was the uncertainty in the meteor position provided by MetRec (ii).

To analyse this error source, it was checked whether the pixel locations of the zeroth-order meteor provided by MetRec pointed to the exact position of the meteor on the frames. After having conducted this analysis on a diverse set of events, it is still unclear whether MetRec provides information about the position of the zeroth-order meteor on ICC8 frame for the meteor's highest point (meteor tail), lowest point (meteor nucleus) or brightest point. Looking at the top-plot of fig. 8, it seems that MetRec tracks the highest point of the meteor's streak in ICC8 frame; by contrast, MetRec provides the location of the lowest meteor's point in the frame of event 17/04/2015 01:41:45 (bottom of fig. 8). The result of our study suggests there is uncertainty in the position of the zeroth-order meteor provided by MetRec. This uncertainty in the input data propagates into the wavelength calibration, specifically affecting step (I) in section 3.1.1, and represents a primary source of wavelength error.

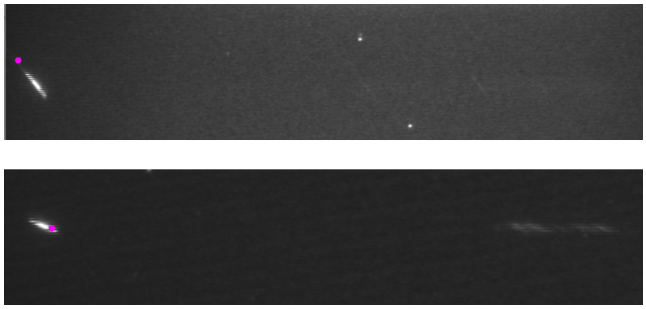

FIGURE 8: *Top-plot*: Event for which MetRec provides the position of the meteor's highest point in ICC8. *Bottom-plot*: Event 17/04/2015 01:41:45, for which MetRec provides the position of the meteor's lowest point in ICC8. The purple dots represent the location of the meteor as estimated by MetRec.

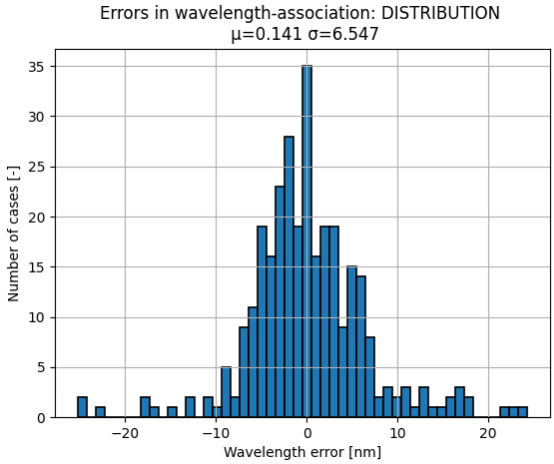

FIGURE 9: Distribution of the wavelength errors for all the 355 visible events analysed. Term μ represents the arithmetic mean and σ the standard deviation of the errors (expressed in nm).

Distribution. Figure 9 shows the distribution of the wavelength errors. For around 90% of the 355 calibrated spectra, the error in the wavelength association to spectral lines is below 10 nm, while for 100% of the cases, the wavelength error does not exceed 27 nm (in absolute value). The former pipeline, instead, produced a calibration box (shown in fig. 12) centred around the spectrum only in around 50% of the cases, and even in those cases the wavelength error at times exceeded 20 nm. These results confirm the superior quality of the newly implemented wavelength calibration pipeline compared the former MRG pipeline, both in terms of reliability and accuracy.

Figure 10 shows how the distribution of wavelength errors correlates with different meteor's entry conditions. Based on this analysis, it was possible to conclude that the distribution of wavelength errors has no correlation with the meteor's magnitude and little with its entry speed, while it shows correlation with the meteor's entry direction. Particularly, the closer the entry direction to the horizon (closer to 90 deg), the worse the error in wavelength calibration. This can be explained considering that an inclination of the entry closer to the horizon increases the difficulty in the retrieval of the meteor's position by MetRec, since the camera can hardly detect the evolution of the meteor's position over time — the uncertainty of MetRec recordings increases, and so do the wavelength errors. The dependence of MetRec positional errors from geometrical effects is also in agreement with findings by Albin et al. (2017). Specifically, the authors concluded that for meteors with greater distances from the center of the camera's FOV and with smaller length of the meteor in the image (as in case of meteors whose angles are close to the horizon), the expected meteor positional errors are larger.

Effects. Errors in wavelength calibration negatively affect the accuracy of the meteoroids' composition retrieval from meteor spectra. In fact, the procedure for the inference of meteor spectra's chemical composition (explained in section 4) requires highly accurate knowledge of the wavelength vector associated to the observed spectral profile. Any error in the wavelength vector can hamper the correct estimation of the abundance of all elements populating the spectrum. An example of this is seen in fig. 11: for the case in which the calibrated spectrum was affected by a wavelength error of 11.8 nm (*left* plots), the spectral analysis routine underestimated the abundance of Mg and O; by contrast, after correcting the spectrum for the wavelength error, the Mg and O spectral features were more accurately estimated, as suggested by the green and red lines in the top-*right* and bottom-*right* respectively.

3.1.3. *Improvements to original calibration pipeline*

An important improvement of the new pipeline involved the correction of meteor spectra for the errors in the wavelength calibration. Based on the analysis presented in section 3.1.2, the uncertainties in MetRec readings represent a key source of error during the wavelength calibration. These errors particularly affect the vertical positioning of the calibration box, which should theoretically be centred at the brightest line of the first-order spectrum in ICC8; fig. 12 shows an event affected by this error. To solve these errors, after performing step (VI) of the wavelength calibration, the spectral profile is obtained from the integration of multiple rows within the frame considered. In fact, when considering that the uncertainty in the position values (x_0, y_0) which MetRec provides in .INF files is of 1-2 frames, summing the contribution of multiple rows in the ICC8 frame along the meteor's path allows to correct for the vertical shift. Integrating the spectra over multiple rows also has the positive effect of reducing its noise. The algorithm implemented to perform the row-integration of spectra is in appendix D.

The most important improvement, however, was the enhanced automation and reliability of the newly developed wavelength calibration pipeline. In fact, the original MRG

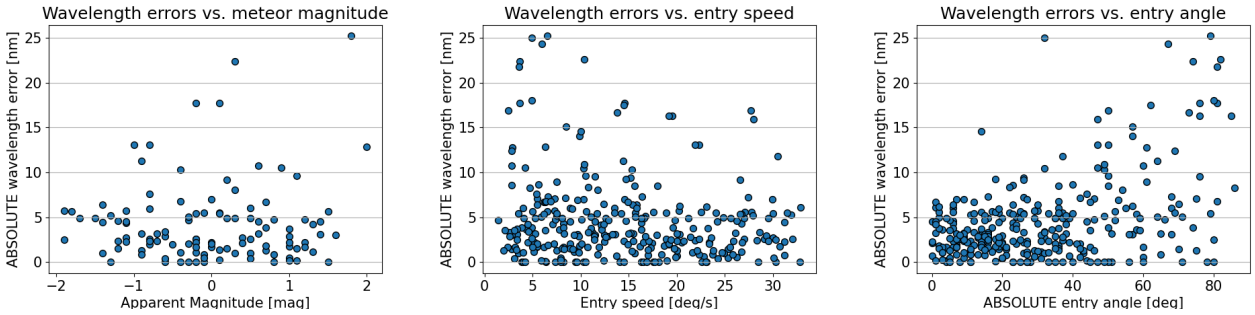

FIGURE 10: Distribution of the wavelength errors as a function of: *left* - meteor's apparent magnitude; *middle* - entry speed; *right* - entry angle (values normalised to 0-90 deg, with 90 deg being the direction along the horizon). All 355 selected events were considered, although the records about the meteor's apparent magnitude were not available for all events.

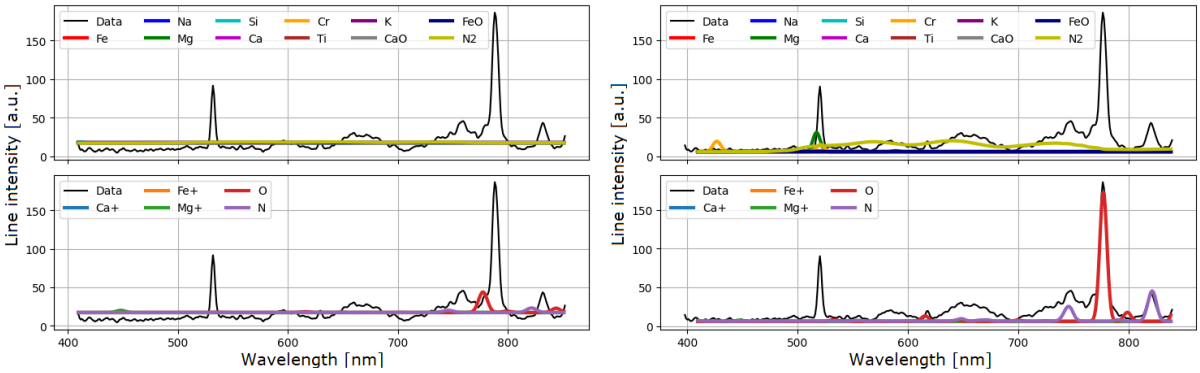

FIGURE 11: Elemental contribution to spectrum resulting from spectral analysis. *Left*: Wavelength error is not corrected. *Right*: Wavelength error corrected. Event: 02/04/2012 03:49:11, with initial wavelength error estimated to be 11.8 nm.

pipeline only worked for roughy 50% of the cases analysed. In the other instances, it generated significant errors in the results, at times beyond 100 nm. Thus, the original pipeline automatically calibrated only a limited set of the events observed; the rest had to be manually calibrated by users, using reference bright lines. This had substantial downsides, especially for time management and accuracy. To satisfy the MRG request of improving the automation of the wavelength calibration process to work for 100% of selected spectra, with errors kept within the order of 10 nm, the wavelength calibration algorithm was successfully re-implemented during this research project.

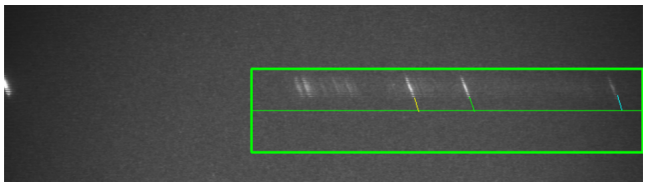

FIGURE 12: Example of a meteor spectrum on ICC8, affected by an error in the wavelength calibration. *Green box*: calibration box; *coloured lines*: position of Mg (*yellow*) and Na (*green*). Event 16/03/2014 23:51:11.

3.2. Atmospheric Calibration

The atmospheric calibration corrects meteor spectra for the wavelength-specific extinction of the whole atmosphere between the meteor and ICC8. Atmospheric extinction varies with the meteor elevation; however, the elevation-dependent nature of the atmospheric correction is often not discussed in the calibration chains, as the same atmospheric correction is generally applied over all the frames observed for a meteor event (as explained in section 1). The atmospheric calibration pipeline developed in this research associates a different correction to each location in the meteor's path, calculating as many correction vectors as many frames. In doing so, this atmospheric calibration returns the spectral information of the meteoroid at the point in the sky where the ICC8 observation occurs. The pipeline developed in this research is described in the following sections.

3.2.1. Methodology: Altitude-dependent approach

The aim of the atmospheric calibration is to correct each meteor spectrum observed by ICC8 for the atmospheric extinction which affects the light transmission from the meteor to ground. To do so, the pipeline associates a correction vector to each observed spectrum; specifically, the vector provides, for each spectral feature of the observed meteor spectrum, a scaling factor to return the feature's

appearance outside the atmosphere. Atmospheric correction vectors are calculated following the extinction law in Appenzeller (2012), as shown below:

$$\textbf{Correction vector} = \frac{\mathbf{F_{0,met}}}{\mathbf{F_{met}}} = \frac{1}{\exp\left(\frac{-\mathbf{b_{met}}}{\cos(\theta_{met})}\right)} \tag{7}$$

Here, $\mathbf{F_{met}}$ represents the intensity of each feature of the observed meteor spectrum, $\mathbf{F_{0,met}}$ the intensities of the true (atmospheric-corrected) spectrum, θ_{met} the Zenith angle of the observed meteorrelative to ICC8, and $\mathbf{b_{met}}$ the atmospheric optical thickness; $\mathbf{b_{met}}$ is a vector varying with wavelength. The atmospheric optical thickness is a coefficient specifying the attenuation of light through the atmosphere. In this study, only the contributions of aerosols' extinction and gas molecules scattering were considered for the estimation of the optical thickness.

In case of gas molecules' scattering-only extinction, the optical thickness ($\mathbf{b_{sca}}$) is obtained as defined below:

$$\mathbf{b_{sca}} = N_{gas} \cdot \sigma_{\mathbf{sca}} \tag{8}$$

with N_{gas} the column number density of gas molecules and $\sigma_{\mathbf{sca}}$ the scattering cross section of gas molecules. N_{gas} and $\sigma_{\mathbf{sca}}$ are obtained using eq. (9) and eq. (10) below, considering a condition of hydrostatic equilibrium.

$$N_{gas} = \frac{p_{bottom} - p_{top}}{m_{gas} \cdot g} \tag{9}$$

$$\sigma_{sca}(\lambda) = \frac{24\pi^3}{N_L^2} \frac{(n^2-1)^2}{(n^2+2)^2} \frac{(6+3\delta)}{(6-7\delta)} \frac{1}{\lambda^4} \approx \frac{C}{\lambda^4} \tag{10}$$

Terms m_{gas} and g are the mass of a gas molecule (obtained for dry air conditions, molar mass of 28.96 g/mol) and the gravitational acceleration (9.806 m/s^2). Terms p_{bottom} and p_{top} are the pressures at the top and bottom of the atmosphere. In eq. (10), n is the gas refractive index (assumed constant), N_L the Loschmidt's number ($2.54743\,10^{25}$ m^{-3}) and δ the gas depolarization constant (0.03 for terrestrial air, ignoring the λ-dependence).

To account for the aerosol optical thickness, the NASA's AERONET database was used. The database used for this purpose and the calculation of the total optical thickness, considering both the gas molecules and aerosols contribution, is investigated further in appendix E.

Figure 13 shows the parameters considered as part of the newly implemented atmospheric calibration pipeline. In this sketch, the values of $\mathbf{b_3}$ (i.e. optical thickness vector at the meteor's location) and θ_{meteor} (i.e. the Zenith angle of the observed meteor) change according to the meteor's elevation. This elevation-dependent approach represents the key feature of the newly implemented atmospheric calibration pipeline: by correcting for the different extinctions taking place while the meteor travels through different elevations in the atmosphere, the estimation of line intensity estimations can be improved by more than 20% for low-wavelength features, as discussed in section 3.2.3. Depending on the meteor's elevation (both

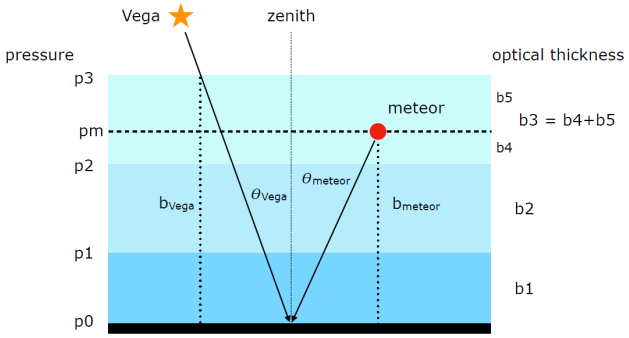

FIGURE 13: Sketch showing the role of optical thickness ($\mathbf{b_3}$) and Zenith angle of observed meteor (θ_{meteor}). Both parameters are used in the formulation of the atmospheric calibration of ICC8 observations of meteors and bright stars (e.g. Vega). Illustration by Dr. D. Stam.

angle above horizon and elevation from ground) at the time when the spectrum is observed, the correction vector changes. Consequently, the atmospheric calibration outputs one correction vector per ICC8 frame recorded.

To get the elevation-varying parameters needed in the elevation-dependent atmospheric correction formulas, a U.S. 1975 Standard Atmosphere was assumed. In particular, what is needed is the pressure variation with height, i.e. p_{top}, while g and n were approximated as constants between the troposphere (where ICC8 is located) and thermosphere (where the meteor observation occurs). The pressure at the height of ICC8 was calculated using standard tables and was the same for each meteor event. By contrast, p_{top} was calculated using the equation:

$$p = p_0 \cdot \left(1 - \frac{L \cdot h}{T_0}\right)^{\left(\frac{g \cdot M}{L \cdot R_0}\right)} \tag{11}$$

where p_0 is the s.l. standard pressure (101325 Pa), L the temperature lapse rate (9.76 K/km, dry air), T_0 the s.l. standard temperature (288.16 K), M the molar mass (0.029 kg/mol, dry air), and R_0 the universal gas constant (8.314 J/(mol·K)).

Three major assumptions were considered for the development of the atmospheric calibration routine. First, a double-layer standard atmosphere (U.S. 1975 Standard Atmosphere) was considered; the first atmospheric layer was fixed at ICC8' height from ground (2395 m), while the location of the second layer varied depending on the meteor's location at the time of the meteor frame acquisition. Second, it was assumed that the atmospheric extinction was only affected by aerosols and gas molecules' scattering; absorption and reflection from water vapour, ozone or other agents were not considered. Third, a condition of dry air was assumed for calculating gas molecules' mass and air pressures.

To first order, these assumptions do not significantly bias the results' accuracy (private communication with Dr. D. Stam). Moreover, the newly implemented atmospheric calibration improved the MRG calibration pipeline, since

this originally lacked any type of correction for the atmospheric extinction. The case study results discussed in section 3.2.3 show the significance of the improvement.

3.2.2. *Validation: TAPAS*

The routine developed to perform the atmospheric calibration was validated using TAPAS[3]. TAPAS is a web-based software which allows users to compute the atmospheric transmission in the line-of-sight to a target with known sky coordinates (Bertaux et al., 2014). Having provided the celestial coordinates of the target body and the observation date, TAPAS computes the atmospheric transmittance from the body in space to the observatory specified. The validation was performed by comparing the atmospheric transmission from TAPAS to that provided by the atmospheric calibration routine (inverse of **Correction vector** in eq. (7)), for same event and observational setup.

Vega was selected as the validating target. This A0Va star has apparent magnitude of +0.026 and its spectrum is visible in several ICC8 frames. Four test events, showing good visibility of Vega spectrum in ICC8, were considered for the validation; these were also successively used for the sensitivity curve calculation (explained in section 3.3).

Results from two of the events chosen for the validation are shown in fig. 14. Their behaviour exemplifies the behaviour of all other test events used for the validation. From fig. 14, it is possible to see that the atmospheric transmittance computed by TAPAS (*red*) agrees to great extent with the results of the atmospheric calibration process developed (*blue*). Common points of distinction between the two results are found in the dips visible in TAPAS results. These dips are mostly caused by the absorption from particles in the atmosphere, which is not considered in our atmospheric calibration pipeline. The smoother dip around 600 nm is linked to the ozone absorption; the profound dips around 750-780 nm are linked to oxygen absorption; other dips are linked to water vapour, which has significant day-to-day variation. Differently than gas molecules' scattering, the contributions of ozone and water vapour absorption on atmospheric extinction have large variability over time; they are harder to approximate through mathematical modelling so it was decided not to include them in this first study. Their addition is however to consider for future work.

Although TAPAS provides more accurate results, as it also accounts for absorption of particles in the atmosphere, the computation of the atmospheric transmission by TAPAS takes significantly more time compared to our atmospheric calibration routine. TAPAS requests users without this software license to provide the input information necessary for the atmospheric transmission calculation (date, observatory, celestial coordinates) via a form; then, TAPAS performs the requested simulation. At the end of each simulation, TAPAS sends the results via email. The entire process, from the form submission on TAPAS website to the reception of the results via email, takes ≈10 min — this makes the use of TAPAS for atmospheric correction unpractical for analyses of large sets of events. By contrast, results for the same events are obtained by our newly developed MRG atmospheric calibration in ≈10 sec. Also, TAPAS does not account for the dependence of atmospheric extinction with height. In fact, it only considers the right ascension and declination of the target body and does not correct for bodies moving within the atmosphere.

[3] TAPAS web-based service is accessible through this link: `http://cds-espri.ipsl.fr/tapas/data?methodName=viewForm`

3.2.3. *Improvements to original calibration pipeline*

The original MRG calibration pipeline did not include corrections for atmospheric extinction. Consequently, the intensities of features calibrated with that pipeline were underestimated. Low-wavelength features in visible spectra were the most affected, since atmospheric extinction corrections are most significant at low wavelengths. To show the improvements which the atmospheric calibration pipeline developed can have on CILBO spectral observations, first we decided to present the case of Elnath, a bright star with a known spectrum. Figure 16 compares the reference spectrum of Elnath recorded by the Space Telescope Imaging Spectrograph (STIS) on board the Hubble Space Telescope (*red*), with the spectrum of Elnath star observed by ICC8 (*blue*), before and after atmospheric calibration. One can appreciate how the application of the atmospheric calibration increases the intensity of spectral features, especially towards the lower wavelengths, thus resulting in better agreements between the reference and observed Elnath spectra. Moreover, fig. 15 quantifies the effects of applying atmospheric calibration on the elements' number density estimations for two frames of a case study: meteor recorded on 01/06/2012 22:51:00. Looking at elements emitting at low wavelengths, like Fe and Ca which have the multiplet 2 emitted at 375 nm and 422 nm respectively, the application of the atmospheric calibration uncovered a significant increase over the frames; on average, Fe and Ca number densities were subject to an increase greater than 10% over each frame, if compared to the estimations done without atmospheric correction.

In this study, an elevation-dependent atmospheric calibration pipeline was implemented; this pipeline calculates as many correction vectors as many frames ICC8 captures during a meteor event, thus associates a different correction to each location in the meteor's path. Figure 17 investigates how the *elevation-dependence* of the atmospheric correction improves the accuracy of the original pipeline. The figure shows the meteor spectrum of frame 34 recorded by ICC8 for the 01/06/2012 case study. The *red* line shows the spectrum if a unique correction was applied over the total image and hence the frame-by-frame variation of atmospheric extinction was not considered; the *blue* line, instead, shows the spectrum after calibration for

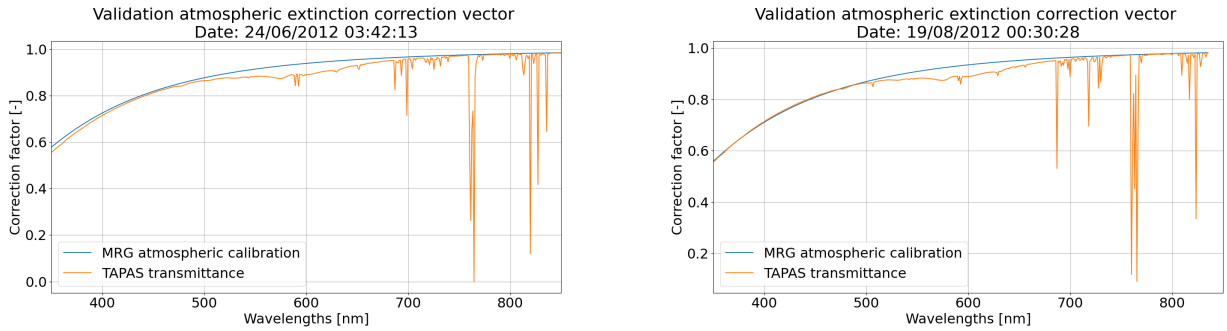

FIGURE 14: Atmospheric transmission in function of wavelength, for two of the events used for the atmospheric calibration validation. Comparison between TAPAS results (*red*) and results obtained using atmospheric calibration process developed (*blue*).

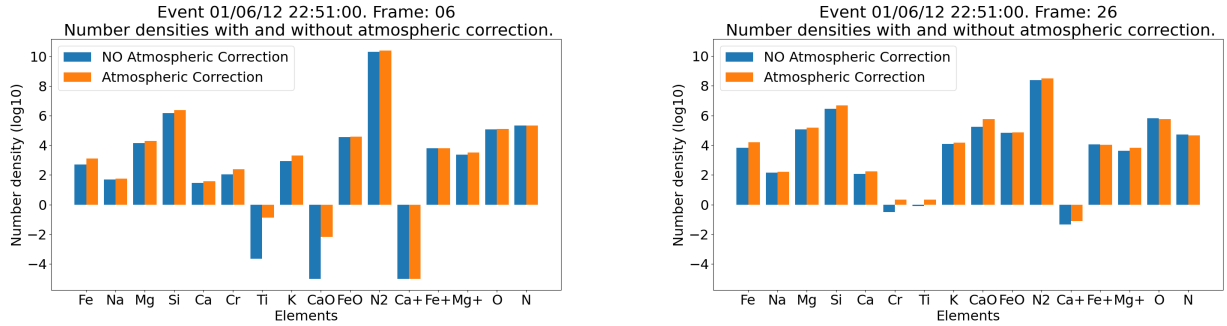

FIGURE 15: Elements' number density for frame 06 (*left*) and 26 (*right*) for event 01/06/2021 22:51:00. *Blue*: No atmospheric correction applied on the spectrum. *Red*: Atmospheric correction applied.

the specific elevation at which the meteor was observed. The results show that the elevation-dependent correction improved the line intensity estimation by an average of 20% for spectral features below 400 nm; considering for example the Fe I (2) emission at around 375.5 nm, the features experiences an increase in line intensity of around 27%. These changes in the line intensities reflect in a different estimation of meteoroid composition compared to cases in which the elevation dependence of the atmospheric correction is not considered. The significance of these results shows the importance of using an elevation-dependent approach which considers the variation in atmospheric extinction as the meteoroid moves through the atmosphere.

3.3. Spectral Sensitivity Characterisation

The last process of the calibration pipeline is the spectral sensitivity calibration. This process adjusts the intensity of the individual spectral lines based on ICC8 spectral sensitivity curve, which displays the instrument's efficiency to record signals at specific wavelengths. The characterisation of ICC8 spectral sensitivity curve resulted from the processing of ICC8 observations of star Vega (α-Lyrae), using the methodology described in section 3.3.1. The validation of the spectral sensitivity curve was performed using spectra of well-known bright stars observed by ICC8, including Deneb, Elnath and Castor (section 3.3.2). Improvements brought by the new sensitivity calibration to the original calibration pipeline are listed in section 3.3.3.

3.3.1. *Methodology: Vega observations from CILBO*

The process of spectral sensitivity calibration corrects spectra observed by ICC8 for the instrument sensitivity curve, according to the relation below:

$$\text{Calibrated spectrum} = \frac{\text{Spectrum observed by ICC8}}{\textit{ICC8 sensitivity curve}} \quad (12)$$

The *ICC8 sensitivity curve* obtained in this study is in fig. 18. The curve resulted from the comparison between the true spectrum of Vega (reference spectrum in fig. 19), obtained from the STIS instrument on board of the Hubble Space Telescope, and ICC8 observations of Vega (observed spectrum in fig. 19): the difference in intensity between features at same wavelength in the reference and observed spectrum gives the ICC8 sensitivity at that wavelength.

According to Buil (2019), the spectrum of a target observed by the same instrument varies across the different dates of observation, even though the target's true spectrum stays approximately constant. In this project, this was noted for Vega's spectrum, which showed differences in the intensity among the different observations of the star's spectrum. These changes depend on several factors, among which the variability in the background luminosity and atmospheric conditions. For this reason, the observed spectrum to compare with the reference spectrum was the result of a median over four good-quality observations of Vega, i.e. four observations in which the first-order spectrum of Vega star was within the ICC8's FOV and had high SNR. By considering different observations for

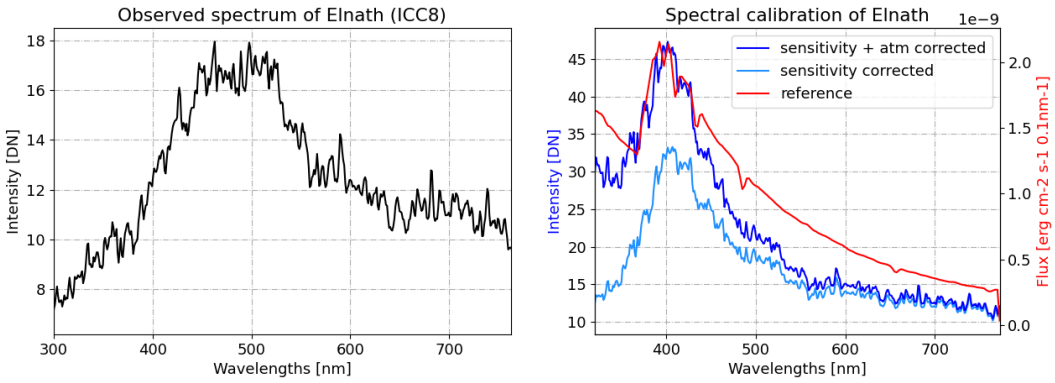

FIGURE 16: *Left*: Spectrum of Elnath as observed from ICC8. *Right-light blue*: Elnath spectrum observed by ICC8, before atmospheric calibration. *Right-blue*: Elnath spectrum observed by ICC8, after atmospheric calibration. *Red*: Reference spectrum of Elnath recorded by STIS outside of atmosphere.

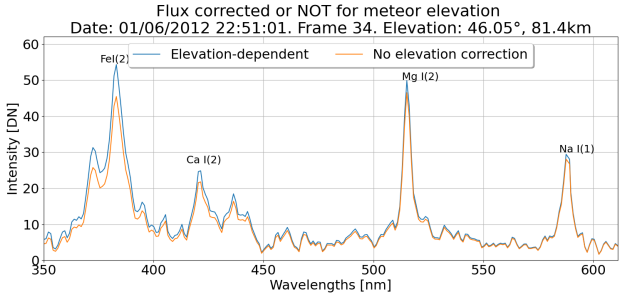

FIGURE 17: Spectra before and after altitude correction. *Blue*: Altitude-dependent approach. *Red*: No altitude-dependent correction. Event 01/06/2012 22:51:00.

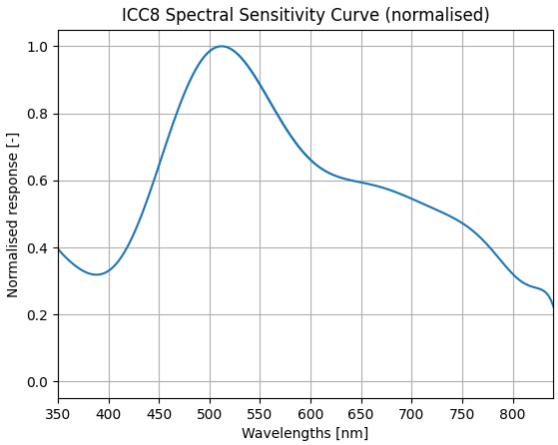

FIGURE 18: ICC8 spectral sensitivity curve, normalised and limited to a wavelength range from 350 nm to 840 nm.

the estimation of the observed spectrum, the changes in intensity are averaged out and the result is a more representative spectrum. The dates of the observations used are: (i) 24/06/2012 03:42:13; (ii) 19/08/20120 00:30:28; (iii) 19/09/2012 22:16:46; (iv) 05/07/2013 03:35:39.

The procedure used for ICC8 spectral sensitivity curve estimation is schematised in fig. 20. This is divided in three parts: (I) processing of ICC8 observed spectra, (II) comparison of the reference and observed spectrum, and (III) final adjustment of the sensitivity curve.

(I) The first part of the processing of ICC8 observed spectra involves the radiometric and wavelength calibration of the four ICC8 observations of Vega spectrum, following the procedures discussed in section 2.3 and section 3.1.1. Next, the spectra are corrected for atmospheric extinction. The correction depends on the direction of observation, which differs per case: the four Vega spectra were all observed at different elevation angles, thus affected by different extinction. The final observed spectrum is the median of the four calibrated spectra.

(II) In the second part of the estimation scheme, the final observed spectrum is divided by the reference spectrum obtained by STIS. The comparison between the two spectra is visualised in fig. 19.

(III) In the third step of the processing of ICC8 observed spectra, the outcome of this ratio is adjusted to a smoothed and normalised, unit-less curve. To smoothen the response curve, averaging out the noise and absorption peaks in both spectra, the curve resulting from step (II) was fitted, using a least-squares polynomial fit (power series) of order twelve. The final instrument response curve is the fitted spectrum after normalisation, using the min-max technique (Patro and Sahu, 2015).

3.3.2. *Validation: Use of bright stars*

To validate the ICC8 sensitivity curve (visualised in fig. 18), the spectra of bright stars, observed by ICC8 and sensitivity-calibrated following eq. (12), were compared to their corresponding reference spectra obtained from catalogues. The bright stars used for the validation are Deneb, Elnath and Castor, whose reference spectra were

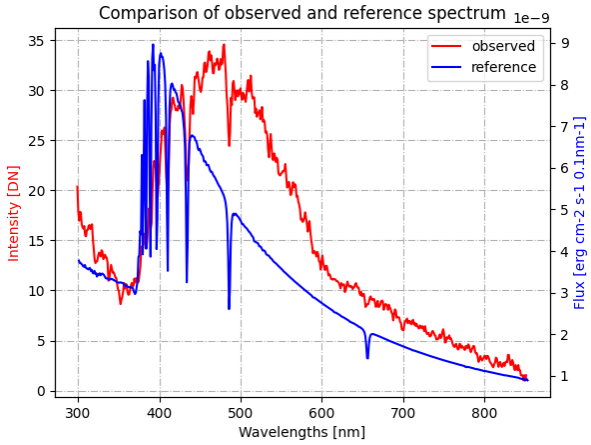

FIGURE 19: Reference Vega spectrum from STIS (*blue*) and spectrum observed from ICC8 (*red*), used for ICC8 sensitivity curve estimation.

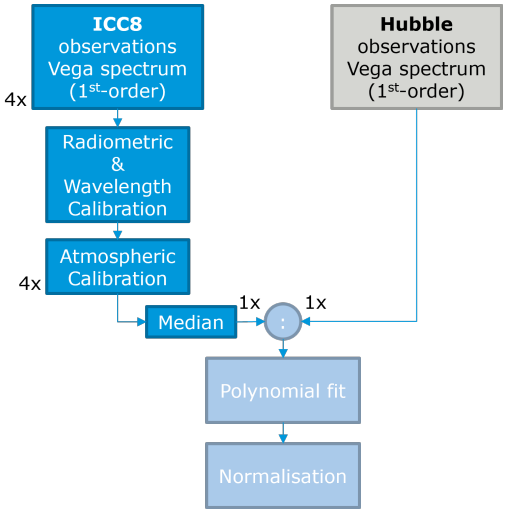

FIGURE 20: Schematic of the steps followed in estimation of ICC8 spectral sensitivity curve.

obtained from the HyperLeda catalogue[4].

The results of this validation are shown in fig. 16 and fig. 21. These confirmed the validity of the estimated ICC8 sensitivity curve for the sensitivity calibration of celestial bodies observed from ICC8. For all the cases considered, in fact, the calibrated spectra of the bright stars observed from ICC8 resemble the behaviour of the corresponding reference spectra (observed outside of the atmosphere), reported in catalogues such as HyperLeda[4] and CALSPEC[5] . Moreover, all the spectra used for the validation were observed at different dates and times — the agreement between reference and calibrated observed spectra for all these different events verified that the sensitivity calibration is not dependent on the specific conditions of the observation date (e.g. background or atmospheric conditions); by contrast, this seems to be a common problem in case of instrument sensitivity curves generated from bright star observations (Buil, 2019).

3.3.3. *Improvements to original calibration pipeline*

In the original MRG calibration pipeline, the spectral sensitivity curve was calibrated in the laboratory, using on-ground observations of lamps with known emission spectra. The estimated curve was limited to wavelengths in the range 400-800 nm. However, an inspection of the spectra observed from ICC8 revealed that a large set of the meteor events selected during data reduction contained features of interest beyond the 400-800 nm range; particularly, Si, Cr and Fe have significant features in the 350-400 nm range, and O and N for wavelengths above 800 nm. For this reason, this project concentrated on a new characterisation of ICC8 sensitivity over a larger wavelength range, specifically 350-840 nm. As the experimental equipment in Tenerife has not been physically reachable for the duration of this project, the new spectral response could not be obtained in a laboratory. Thus, an artificial response curve was generated by processing multiple ICC8 observations of Vega star, as explained in section 3.3.1.

The wavelength boundaries used for the characterisation of the new ICC8 spectral sensitivity curve were chosen based on the absence of significant features beyond the 350-840 nm range and the lower accuracy of the atmospheric correction — the analytical formula used for atmospheric extinction modelling is less reliable when trying to estimate the extinction below 350 nm, due to the higher complexity of the phenomena in the UV.

The re-definition of ICC8 spectral sensitivity curve over a wider wavelength range (350-850 nm) brings a final improvement to the MRG calibration pipeline: the wider and more complete sensitivity curve allows to analyse new features in meteor spectra, and hence more accurately infer meteoroids' compositions. This eventually represents one of the main accomplishments of this project, in the optics of future work in the MRG at ESA.

4. METEOR SPECTRA ANALYSIS

How do different meteoroid-atmosphere interactions, induced by varying atmosphere or meteor entry conditions, reflect on spectral features and affect their analysis?

Addressing this question represented one of the major research objectives of this project, as introduced in section 1. The following sections aim to describe the methodology and main results obtained from the research conducted on this topic. Specifically, section 4.1 explains the methodology used for the meteoroid composition inference from the meteor spectra selected, while section 4.2 and section 4.3 illustrate the main results derived from the study of the correlation between external factors and spectral features for the meteors analysed.

[4] HyperLeda catalogue: http://leda.univ-lyon1.fr/.

[5] CALSPEC Archive: https://archive.stsci.edu/hlsps/reference-atlases/cdbs/calspec/.

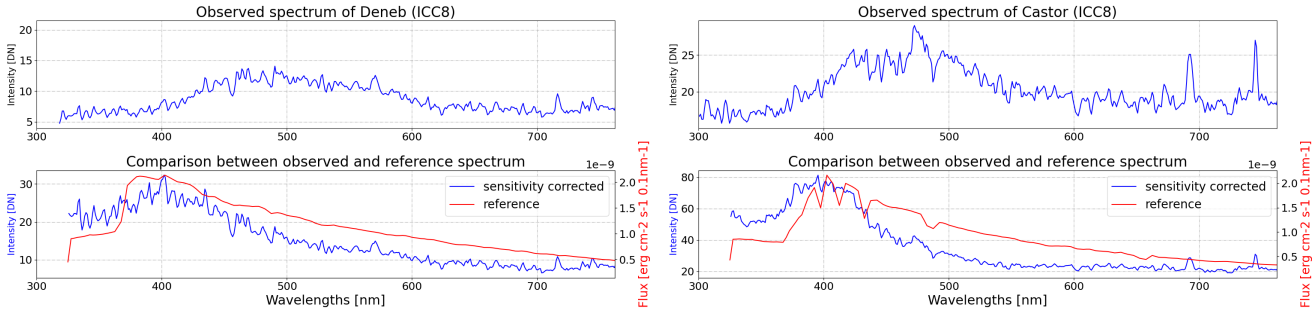

FIGURE 21: Spectra of bright stars Deneb (*left*) and Castor (*right*). *Top*: Observed spectrum before sensitivity calibration. *Bottom*: Spectrum after the complete spectral calibration (instrument sensitivity and atmospheric extinction). In *red*, the reference spectrum of Elnath outside of atmosphere (Hyper Leda catalogue). In *blue*, observed spectra.

4.1. Meteoroid Composition Inference

The chemical composition of meteoroids can be inferred through spectral analysis of meteors observed from ground-based optical cameras. In this study, the spectral analysis primarily aimed at measuring the spectral line intensity and number density of the elements emitted during meteor ablation, along with the temperature at which the meteor's ablation took place. Estimating the contribution of each element to the observed emission spectrum is not trivial, especially because the intensity of each line in the observed spectrum is the result of its interaction with different components; in fact, components such as the continuous emission, nitrogen bands, other elements' emissions and the instrument effects influence the element's intensity at the line position in the *observed* spectrum, and hence bias the interpretation of the element's abundance in the meteor spectrum (Vojácek et al., 2015).

For this reason, the meteoroid composition inference in this study was performed using *synthetic* spectra, where the contribution of each component on the final emission spectrum can be analysed separately, without being influenced by the action of the other components. The synthetic spectra were obtained through a semi-automatic spectral fitting of the observed meteor spectra.

4.1.1. *Methodology: Synthetic Spectra Modelling*

Starting from a radiative transfer model, a synthetic spectrum can be modelled for each radiating element i contributing to the observed emission spectrum, each having a number of radiators N_i associated, when knowing the temperature T at which the element emission happens. The radiative transfer model used in this research for the modelling of the synthetic spectra is:

$$\int_{meteor} \mathbf{F}(\lambda, T) \propto \sum_i N_i(T)\, \mathbf{j_i}(\lambda, T) \qquad (13)$$

$\mathbf{F}$ is the flux vector of the complete spectrum, resulting from the integration over the spatial dimensions of the meteor (i.e. the sum of the spectra of all radiating elements i), λ is the wavelength and $\mathbf{j_i}$ is the vector with the wavelength-dependent emission coefficients of element i. The radiative transfer model used in this research assumes that only emission and no self-absorption happens within the meteor, thus the meteor is modelled as an optically thin gas (optical depth $\tau \ll 1$) in thermal equilibrium.

In eq. (13), the elements' emission coefficients $\mathbf{j_i}$ are retrieved from the PARADE database (described in section 4.1.2). The flux vector $\mathbf{F}$ comes from the meteor observations. The only unknowns of the equation are the element number densities N_i; the scope of the spectral fitting of the observed spectra is to retrieve these values.

TABLE 3: Parameters considered in the spectral analysis routine and type of prior used for the Bayesian inference (Landman, 2020). Abbreviations — STD: standard deviation; U: uniform distribution; G: Gaussian distribution; J: Jeffreys distribution. U_{log}: uniform distribution, for the *logarithm* of the number density.

Parameter (Unit)	*Description*	*Prior*
T_1 (K)	Temperature main spectrum	U(3000, 5000)
T_2 (K)	Temperature second spectrum	U(2000, 15 000)
σ (a.u.)	STD instrumental broadening	U(0,5)
$\Delta\lambda$ (nm)	Wavelength shift	G(-5,5)
b (a.u.)	Background count rate	J(0, 100)
N_i (cm^{-2})	Number density of element i	U_{log}(-5, 25)

The spectral fitting of ICC8 observed spectra, used for the estimation of the number densities of the meteor's radiating elements, is articulated in five main steps.

1) First, the user defines which parameters to estimate through the spectral fitting procedure. An overview of the parameters considered in this research is shown in table 3.

2) The spectral analysis routine retrieves from PARADE the emission coefficients of all elements which we aim to consider in the meteor spectra analysis (table 4). The coefficients are provided at all temperatures in the range 2000-15 000 K, as further described in section 4.1.2.

3) For each radiating element in table 4, the routine models first-guess synthetic spectra. These are obtained combining the parameters in table 3, left free to vary

within defined boundaries (*Prior* in tab. 3). The complete synthetic spectra are then obtained for each combination, by summing the individual elements' spectra.

4) Using a non-linear LSQ approach, an initial solution is obtained. This provides the estimate of all the unknown parameters in table 3, whose combination generates a complete synthetic meteor which best fits the ICC8 observed meteor spectrum. The best-fit LSQ estimates are only an initial solution; thus do not coincide with the final best-fit solution obtained at the end of the routine.

5) The LSQ parameters' estimates are used as initial guesses for the successive Markov Chain Monte Carlo (MCMC). During the MCMC, for each meteor event 1000 iterations are run. Each iteration models a different synthetic spectrum using parameters which are sampled around the LSQ solution via MCMC affine-invariance sampling (described in appendix F). The complete synthetic spectrum which best fits the ICC8 observed spectrum is inferred using Bayesian inference. As explained in appendix G, the Bayesian inference estimates the posterior distribution for all parameters; the results are the parameters for which the complete synthetic spectrum best fits the observed spectrum, thus those for which the posterior is highest.

The use of a MCMC approach in addition to the LSQ estimation, although making the process more computationally expensive, is essential for a more accurate probabilistic inference of meteors' elemental composition. In fact, the MCMC approach allows to properly correct for the effects of noise in spectra, otherwise identified as signal in a LSQ estimation. Moreover, while the LSQ solution is affected by the initial choice of parameters and thus their uncertainties, the posterior distribution sampling in the MCMC intrinsically accounts for uncertainties by marginalising over nuisance parameters (Landman, 2020).

The synthetic spectra generated during the spectral fitting procedure take into account the atmospheric and instrument effects modifying the observation of the source spectra. Ground-based observations are affected by effects like atmospheric extinction, camera's sensitivity and instrumental broadening, which modify the appearance of the meteor spectra observed on ICC8, independently from the source spectra look. For an accurate meteoroid composition inference, these effects need to be applied on synthetic spectra as well. By doing so, the synthetic spectra are comparable to the corresponding observed spectra, thus the spectral fitting is successful. Some of the instrument effects are accounted in the form of parameters to estimate; this is the case for the broadening induced by the finite resolution of ICC8 and its optics (σ), and the background count rate (b). The remaining effects, i.e. atmospheric extinction and ICC8 spectral sensitivity, are applied on the synthetic spectra at the end of step 3) of the spectral fitting routine. Atmospheric extinction and ICC8 spectral sensitivity are obtained following the methodology described in section 3.2.1 and section 3.3.1, respectively.

TABLE 4: Elements which are considered for the meteor spectra analysis, corresponding to radiating species emitted during meteoroid entry based on literature research. These elements belong to the Main and Second spectrum, according to the findings of Borovička (1993); Borovička et al. (2005); Jenniskens (2007).

Main spectrum	Fe, Na, Mg, Si, Ca, Cr, Ti, K, CaO, FeO, N_2
Second spectrum	Ca_{II}, Fe_{II}, Mg_{II}, O, N

The spectral fitting routine developed in this research was in large part an adaptation of the spectral analysis pipeline implemented in the MRG by Landman (2020). Some key improvements were however implemented, specifically in view of our work on the calibration pipeline. The first main improvement concerned the use of the wavelength errors estimated during the wavelength calibration (section 3.1.2) as initial guesses for the wavelength shift parameter ($\Delta\lambda$ in table 3); as a consequence, the parameters estimated during the spectral fitting all ranged below 1 nm and were an indicator of the uncertainty of the wavelength error estimation routine developed. Another important improvement was the possibility to analyse spectra for each individual frame observed, while before only spectra from total images were analysed.

4.1.2. *Plasma Radiation Database*

PARADE is a plasma radiation database, whose primary application is the simulation of the electromagnetic radiation in the Earth's environment (Winter et al., 2006). In the context of meteor spectra analysis, PARADE is particularly useful for the computation of the emission and absorption coefficients of the atoms and molecules electronically excited during a meteoroid entry. The radiation data provided by PARADE (Einstein coefficients, energy levels, atomic masses, etc.) is obtained from literature or resulted from spectroscopic experiments conducted on meteorite samples at the University of Stuttgart's plasma wind tunnel (Löhle et al., 2017).

In the context of this research, PARADE was used to generate a database with the emission coefficients of all radiating elements emitted during meteoroid entry (table 4). The emission coefficients were calculated for each temperature in the temperature range going from 2000 K to 15 000 K, spaced of 50 K, and each wavelength in the range 350 nm to 840 nm, spaced of $\approx$ 0.5 nm. The sampling of the wavelength range was chosen to be equal to half the camera resolution ($\approx$ 1 nm/px). This represented the right compromise between accuracy of PARADE estimations and computational cost: if the wavelength interval is too broad, some emission feature might not be picked, as the wavelength-specific peak of the emission spectrum would not be seen, while too narrow intervals signify substantial increases in computational time.

TABLE 5: Summary of the variables studied during meteor spectral analysis, along with their units of measure.

Variable	*Unit*
Emission coefficient	W/m^3
Number density	cm^{-2}
Line Intensity	DN *or* a.u.
Relative Number Density	-
Relative Line Intensity	-

4.1.3. Variables of Interest in the Spectral Analysis Routine

Various variables can describe a meteoroid composition. The variables of interest for the analysis performed in this study, and presented in section 4.2 and 4.3, are number densities and line intensities. These are summarised in table 5, with their units of measure.

The number density of an element is defined as the value N_i in eq. (13), derived from the contribution of the element to the instantaneous meteor's spectral profile, i.e. the spectrum considered at a specific instant of time (Jenniskens, 2007). Number densities represent one of the parameters estimated within the spectral analysis routine.

The line intensity is the intensity of a peak at a specific wavelength in the spectrum (spectral feature). Line intensities of neutral Mg, Na and Fe are especially useful for meteor spectra classification. In literature, meteor spectra are classified based on the abundance of multiplets Fe I (15), Mg I (2) and Na I (1) (Borovička et al., 2005; Vojácek et al., 2015); these correspond to peaks at 526.9 nm, 518.2 nm and 589.2 nm, respectively.

An element's relative number density is given by the element's number density divided by to the number density of Mg I (2). Similarly, the relative line intensity is the element's line intensity relative to the Mg I (2) intensity.

4.2. The Influence of External Factors

As explained in section 1, the inference of meteoroids' chemical composition from meteor spectra is affected by the different meteoroid-atmosphere interactions ongoing at the time of the meteor observation. Factors other than the chemical composition of the meteoroid (external factors) influence this interaction, thus affecting the appearance of meteor spectra features. The focus of this section is on meteoroid entry speeds and the section aims to answer the following research question:
To which degree do variations in meteoroid entry speed affect the appearance of features in total meteor spectra?

4.2.1. Entry speeds and elemental abundances

Various researchers analysed the impact of meteoroids' entry speeds on meteor spectra elemental abundances, including Borovička (1993); Borovička et al. (1999); Vojácek et al. (2019); Matlovič et al. (2020). An important and common conclusion drawn from all their studies was that the sodium dominance in meteor spectra (Na-rich spectra) is correlated to low entry speeds. Sodium is a volatile element and its dominance in the spectra of low-speed meteors is explained by the low temperatures reached during their ablation — the excitation induced in low-speed bodies is not enough to trigger the emissions of more refractory elements, thus volatile elements dominate their spectra. This suggests that the emission spectra of low-speed meteors do not reflect the true relative elemental abundance in their parent bodies, since the meteor ablation does excite all elements in the meteoroid.

Previous researches on this topic analysed meteors with entry speeds spanning over wide ranges (i.e. 10 km to 70 km/s in Vojácek et al. (2019); Matlovič et al. (2020)). However, their database had a limited number of events with low speeds (lower than 20 events with speed below 20 km/s for the researches above), even though a more populated set would have been of greater interest considering the conclusions drawn. To this end, this project serves as a nice addition to this research area, since it focused on the analysis of meteor events with low entry speeds: among the meteor selected for this project, 198 (of 355) had entry speeds below 20 km/s, and the remainder did not exceed 35 km/s.

ICC8 *total* meteor spectra were analysed; the results of this analysis are shown in fig. 22 and fig. 23. From this analysis, it was concluded that there exists a strong correlation between the meteor's entry speed and the number density of the emitted elements. The correlation is seen for both elements of meteoric origin, such as Fe and Na, and of atmospheric origin, like O and N; however, the trend they follow is distinct. Using a first-order polynomial fit of the data (*black line*), it was then possible to quantify the rate of change of the elements' number densities with speed, relative to the more stable Mg number density. For this estimation, the change in relative number densities (expressed in unit-less, logarithmic scale) was divided to the corresponding interval of meteor speed (in m/s); the result was therefore a value expressed in $(m/s)^{-1}$.

From fig. 22, it is possible to observe that the elements of meteoric origin (i.e. Na and Fe) decrease in number density when the speed of the meteor increases. The behaviour of the Na relative number density (left plot), is in agreement with the conclusions drawn from previous researches about sodium enhancement in low-speed meteor spectra (Vojácek et al., 2019; Matlovič et al., 2020) — a rate of decrease of Na relative number density of about $-10\,(m/s)^{-1}$ was obtained from our analysis. In a similar way, Fe showed a decrease in its relative number density as the meteor speed increased, although of lighter intensity: about $-3\,(m/s)^{-1}$. This agrees with Matlovič et al. (2020) and Borovička et al. (2005), whose research concluded that low-speed meteor spectra are either Na-rich or Fe-rich.

The behaviour of meteoric elements was expected beforehand, if considering that the more volatile elements like Na tend to reach complete emission already when lower ablation temperatures or pressures are reached. Thus, for low-speed meteors, volatile elements are likely emitted through the entire path. By contrast, for fast-

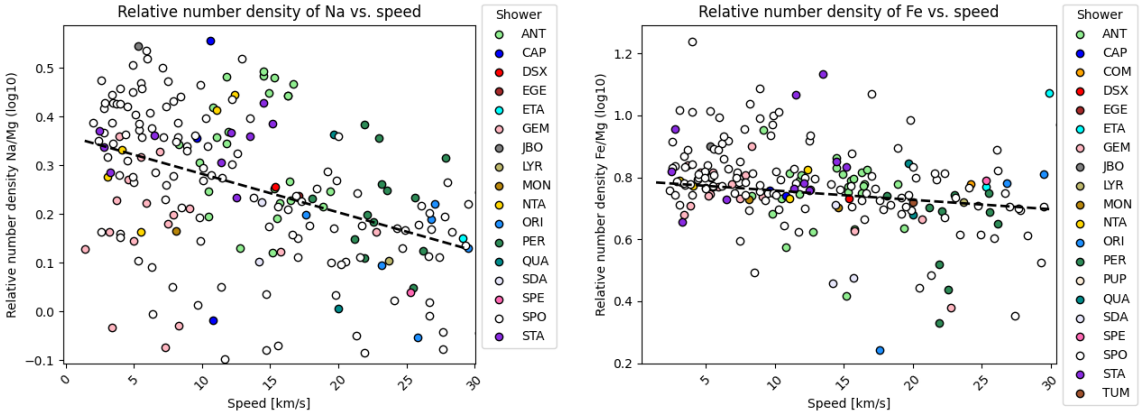

FIGURE 22: Correlation between the *meteoric* elements' number density (relative to Mg) and the meteor speed. *Left*: Na abundance; *right*: Fe abundance. Colors are used to separate meteors belonging to different showers. *Black line*: First-order polynomial fit. Results from the analysis of the *total* spectra of the meteor events selected during Data Reduction (section 2.2).

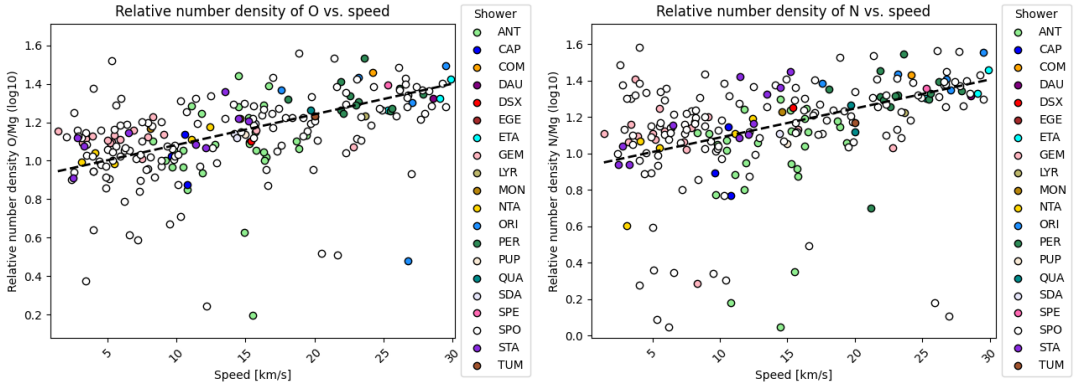

FIGURE 23: Correlation between the *atmospheric* elements' number density (relative to Mg) and the meteor speed. *Left*: O abundance; *right*: N abundance. Colors are used to separate meteors belonging to different showers. *Black line*: First-order polynomial fit. Results from the analysis of the *total* spectra of the meteor events selected during Data Reduction (section 2.2).

speed meteors the volatile element emission happens at higher heights, thus part (or all) of the emission falls outside the meteor spectrum observed from ICC8. Since these emission are not observed through the entire meteor path, their contribution to the *total* spectrum decreases. In high-speed meteors, the part of the spectrum observed from ICC8 has higher abundance of more refractive elements like Mg; this also contributes to the decrease in meteoric elements' number densities relative to Mg.

Differently than meteoric elements, elements of atmospheric nature increase in abundance (relative to Mg) with speed, as visualised in fig. 23. The rate of increase with speed estimated for both O and N coincided to around $+16\,(\mathrm{m/s})^{-1}$. This could be explained considering that the atmosphere has an (almost) infinite reservoir of atoms. Thus, while meteoric elements are emitted and their abundance in the meteoroid decreases, atmospheric ones are constantly replenished in similar amounts. Moreover, with higher speeds the ablation temperatures and pressures increase. These conditions favor the excitation of atmospheric elements, which are therefore emitted in higher amounts — Mg variation with speed is more moderate, thus the result is an increase in the emission rate of atmospheric elements relative to Mg. Finally, this suggests that intensities of elements of atmospheric origin are good measures of the meteor's entry speed, which agrees with past research results by Borovička et al. (2005).

4.3. The Evolution of Spectra along Meteors' Path

A major improvement of the new spectral analysis routine was the possibility to analyse the meteor spectra associated to each individual frame recorded by ICC8. In fact, previous studies from MRG (and in literature) only concentrated on the analysis of the total spectra. Analysing individual frames' spectra has a profound advantage compared to analyses of total images' spectra: it allows to investigate the evolution of meteor spectral features, as that meteor moves through lower layers of the atmosphere, hence as the meteoroid's interaction with the atmosphere varies. In this section, individual frames of meteor spectra collected by ICC8 were analysed. The aim of this analysis was to answer the research question: *How does the variability of meteoroids' interaction with*

the atmosphere correlate with changes in spectral features among meteors generating from the same shower?

4.3.1. *Elements' emission along the meteor's path*

As meteors move towards lower layers of the atmosphere, the meteoroids' interaction with the atmosphere varies. In this research, we are interested in investigating the correlation between variability of the meteoroid-atmosphere interaction and the changes in meteor spectra. To do so, the evolution of individual frames' spectral appearances is analysed in relation to changes in ablation conditions; these include changes in ablation height, ablation temperature and meteor apparent magnitude, caused by different interactions between meteoroids and Earth's atmosphere. The events for which this analysis was conducted were selected among the shower meteors for which a more significant change in the spectral features along the meteor's path in the atmosphere was observed. The process of selection is explained in appendix H.

Moving towards lower heights in the atmosphere, the emission of meteoric features was seen to increase; this was especially the case for features in the UV part of the spectrum, such as Fe I (2), a multiplet of Fe appearing at 375.5 nm. For the events selected for this analysis, the evolution of meteoric elements' number densities along the meteor's path is visualised in fig. 24. At lower heights, the ablation temperature estimated from the spectral analysis routine also experienced an average increase, as implied by the yellow-ward trend towards lower heights in fig. 24. This indicates a correlation between the variations of spectral abundances over the frames and changes in the meteor ablation temperature with height. The slightly different pattern observed for Na (*right* plot) is explained considering that sodium is highly volatile — it starts depleting at higher heights, where the temperatures are lower, and it is fully depleted already before reaching the lowest distance from ground; after reaching its full depletion, its abundance decreases and the evolution with height experiences an inverse trend.

One of the most straight-forward indicators of the variability of meteoroids' interaction within the atmosphere is the change in meteors' brightness. This can be visualised through light curves (*top* plots in fig. 25); in this study, light curves are obtained using the meteors' apparent magnitudes, provided by Metrec. The relation between light curves and the emission of meteoric elements over the meteor's path in the atmosphere is analysed for all the frames' events selected. In particular, attention is posed on Mg emissions, due to its higher stability compared to other elements. Figure 25 presents the results of this analysis for three representative events. There exists a strong correlation between the evolution with height of the Mg line intensities and the frame-by-frame progression of the meteor's light curves — an increase in the meteor's apparent magnitude over the frames is accompanied (with a small time offset) by an increase in the Mg line intensity. This correlation was examined using the Spearman's rank correlation coefficient, which assesses the strength and direction of the monotonic relationship between two parameters (Artusi et al., 2002); the *stats* package in Python has the Spearman's method implemented. An average correlation coefficient of 0.69 was obtained for Mg, considering all events selected[6]. For other meteoric elements (e.g. Na and Fe) the correlation was around 0.50 (0.48 and 0.49).

As the procedure to obtain calibrated meteor spectra is substantially more complex than the pipeline used for light curve estimation, the correlation of Mg line intensities with meteor brightness is extremely interesting in the context of preliminary events' selection. For example, consider the case of researchers interested in studying the emission of meteoric elements at a specific layer in the atmosphere: after inspecting the meteors' light curves, they could reduce the initial set of spectra to a handful of interesting events, simply by picking those for which the meteor brightness is strong at the layer's height range. This way, they would not need to apply the computationally expensive spectral analysis and calibration on all events.

4.3.2. *Evolution of shower meteor's emissions over years*

Elements emitted by meteoroids belonging to the same stream and observed during the same shower event are expected to have similar abundances in meteor spectra. In fact, meteoroids from the same stream generate from the same parent body and go through a similar space radiation exposure. Moreover, it is expected that the interaction with the different atmospheric layers is comparable among shower meteors. However, the questions arose: *Would the elements' emission patterns change if considering meteoroids of the same stream but observed at different times? How does the variability of these meteoroids' interaction in space affect the corresponding meteor spectra?*

To address these points, spectra of meteors belonging to the same shower, but for which the observation happened in different years, were analysed. Meteors belonging to the ANT (Radiant Antihelion) and GEM (Geminids) shower were chosen, for which 36 and 24 events were observed, respectively, from 2012 to 2017.

The evolution over time of the line intensities of the *total* spectra meteoric emissions is shown in fig. 26 and 27; an average decrease in the line intensities of Mg, Fe and Na is traceable over time, for both GEM and ANT meteors. A possible cause behind these observations is the different exposure to space radiation (both cosmic and solar) which meteoroids observed at different times go through. The interaction with the space environment, in fact, determines the depletion from meteoroids' surfaces of elements, especially volatile ones (Borovička et al., 2005). Longer exposures to space radiation thus results

[6] The significance of the correlation was p-value tested for all events. This verified that the risk that the correlations were obtained by chance is less than 5%, i.e. significance level $\alpha = 0.05$ (Feigelson and Babu, 2013)

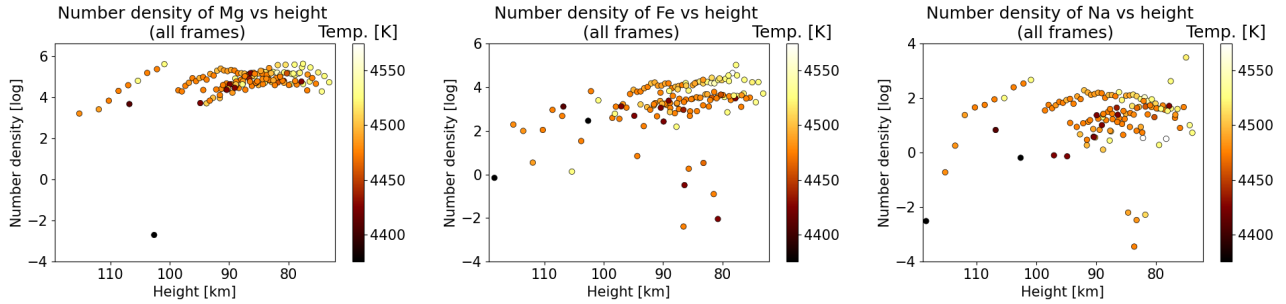

FIGURE 24: Number density of meteoric elements in function of the height. *Left*: Mg I (2) line intensity; *middle*: Fe I (2); *right*: Na I (1). Events analysed are *individual frames*' meteor spectra of shower meteors. The colorbar gives information about the ablation temperature.

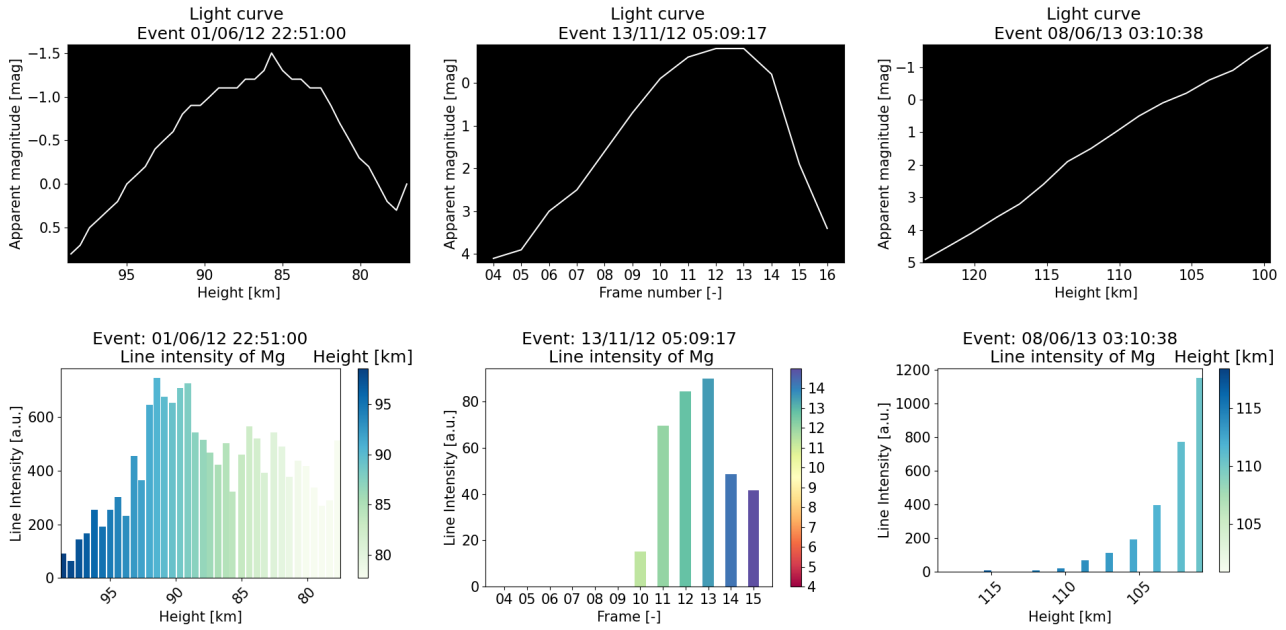

FIGURE 25: Light curves (*top*) and the frame-evolution of the Mg line intensity for the corresponding spectrum (*bottom*).*Left*: Event 01/06/2012 22:51:00. *Middle*: Event 13/11/2012 05:09:17. *Right*: Event 08/06/2013 03:10:38.
Please note that for the middle case, no height information is available from the MRG database, thus the frame number is provided to inform about the meteor's path in the atmosphere: as the meteor moves towards lower heights, the frame number associated increases.

in larger elements' depletion before the meteoroids enter the atmosphere; consequently, the abundance of meteoric elements excited during atmospheric ablation reduces.

The exposure of the stream to space radiation is however not the only possible, nor the most plausible, explanation behind these observations. A more plausible explanation is that the shower meteors observed in the different years have come from different filaments of the meteoroid stream. Meteoroids from different filaments of the same stream have different dynamical evolution and can impact the Earth's atmosphere at different arcs of its orbit (Neslusan and Hajduková, 2018). Also, they can be ejected at different times and from different layers of the parent body; hence, they can have a different composition. Therefore, to better interpret the yearly evolution of the spectra of meteors, the dynamical evolution of their meteoroid stream should also be investigated.

5. CONCLUSIONS

This research has two main goals: assess to what degree external factors influence shower meteors' spectra and improve the calibration pipelines used for their correction. Regarding meteor spectra calibration, an automatic procedure for the elevation-dependent atmospheric calibration was developed and validated. The output of this calibration pipeline are correction factors, which perform a correction of the observed spectra for the atmospheric extinction influencing meteor spectra observations.

The new elevation-dependent approach allows to correct the meteor spectra for the variation in atmospheric extinction as the meteoroids travel within the atmosphere. The use of an elevation-dependent atmospheric

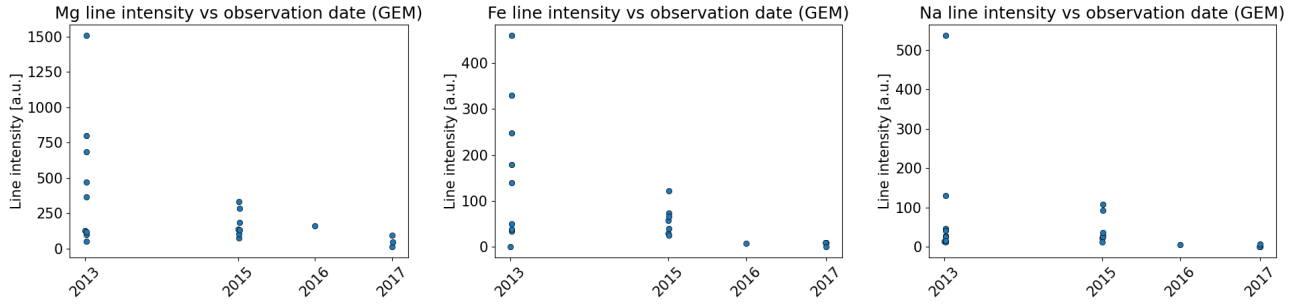

FIGURE 26: Line intensity of meteoric elements in function of the year of observation of the event. *Left*: Mg I (2) line intensity; *middle*: Fe I (15); *right*: Na I (1). Events analysed are *total* meteor spectra of GEM shower.

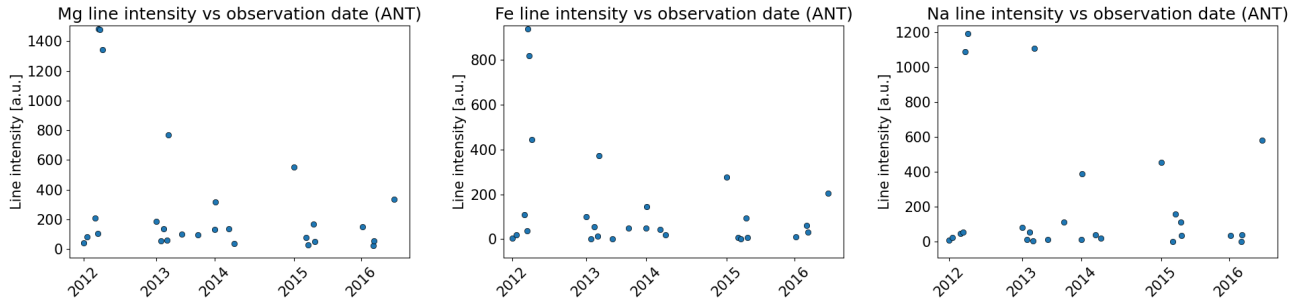

FIGURE 27: Line intensity of meteoric elements in function of the year of observation of the event. *Left*: Mg I (2) line intensity; *middle*: Fe I (15); *right*: Na I (1). Events analysed are *total* meteor spectra of ANT shower.

calibration brings significant advantages for the accuracy of both the calibration pipeline and the meteoroids' composition inference. Specifically, we demonstrate that this correction can improve the line intensity estimations by more than 20% for spectral features at wavelengths below 400 nm, compared to cases in which the elevation dependence of the extinction variation is not taken into account; this reflects in better compositional inferences in meteor spectral analyses, at negligible a cost in computational time (<1 sec per event). The significance of these results shows that applying an elevation-dependent atmospheric calibration is preferable over the standard approach for atmospheric correction, which does not account for the extinction variation at the different times of meteor observation. We therefore encourage researchers in meteor spectroscopy to consider the implementation of such an elevation-dependent atmospheric correction in their work.

In this project, 355 first-order meteor spectra collected between 2012 and 2018 by ICC8, an image-intensified CCD video camera in CILBO observatory, were analysed. The spectral analysis of these events investigated the correlation between meteoroid-atmosphere interactions and spectral features abundances; this was approached through two diverse studies.

In the first study, the influence of entry speeds on the emission of meteoric and atmospheric elements was investigated: the number densities of Na and Fe (meteoric origin), and O and N (atmospheric origin) relative to Mg were analysed in function of their meteor's entry speed. A rate of decrease of about $-10\,(\mathrm{m/s})^{-1}$ was calculated for Na number density relative to Mg; moreover, our results showed a decrease in Fe relative number density with speed of around $-3\,(\mathrm{m/s})^{-1}$. The difference was linked to the lower excitation potential of Na compared to Fe, meaning that Na require less energy to radiate (Borovička et al., 2005). The analysis performed on elements of atmospheric origin gave an opposite outcome: both N and O relative number densities showed an increase with speed of $+16\,(\mathrm{m/s})^{-1}$, irrespective of their volatility.

Altogether, the conclusions from this study showed the existence of a strong correlation between meteors' speeds and number densities, as already pointed out in the researches on *meteoric* elements' emissions by Matlovič et al. (2020) and Vojácek et al. (2019). However, our research demonstrated that the type of correlation depends on the nature of the element (atmospheric or meteoric). Furthermore, the correlation between number density changes with speed and meteoric elements' volatility shows that meteor speeds can influence the appearance of their spectra; this implies that meteoroid compositions inferred from meteor spectra should always be interpreted taking into account the meteor speed.

The second study focused on the evolution of spectral features over time and space. Firstly, we analysed the changes in elements' emission for meteors of the same

showers, GEM and ANT, but observed over different years. Both GEM and ANT meteors revealed a mean decrease per year in meteoric elements' number densities — ANT meteors showed mean decrease per year in Mg number density of 10%, 18% for Fe and 12% for Na; GEM meteors had a mean decrease per year of 8% for Mg, 18% for Fe and almost null for Na. From these results, we learnt that meteors belonging to the same shower (thus same parent body) are not necessarily homogeneous in their composition and the spectra show differences based on the meteoroid stream filament observed. This implies that meteor spectroscopy requires complementary dynamic studies for a successful association of an observed shower meteor spectrum to its parent body.

Finally, individual frames of meteor events were analysed. This analysis showed that elements belonging to the same meteor have different emission patterns depending on the height at which the observation occurs. Our analysis concluded that the variations in emissions over the frames are primarily caused by height changes in ablation temperatures, which excite different elements based on their volatility and their residual abundance at that height. Most state-of-the-art research, including studies by Jenniskens (2007), Borovička et al. (2005) and Rudawska et al. (2020), analyse only the total meteor spectra, in which the variability per height of the spectrum is lost. This research, however, showed that studying the evolution of emissions over the frames can uncover important information about the meteoroid structure and ablation process, otherwise hidden from analyses on total spectra. Future researchers should thus consider contributing to the study of the evolution of meteor spectra along the meteoroid's path in the atmosphere.

REFERENCES

T. Albin, D. Koschny, S. Molau, R. Srama, and B. Poppe. Analysis of the technical biases of meteor video cameras used in the CILBO system. *Geoscientific Instrumentation, Methods and Data Systems*, 6(1):125–140, 2017. URL https://doi.org/10.5194/gi-6-125-2017.

I. Appenzeller. *Introduction to Astronomical Spectroscopy*. Cambridge Observing Handbooks for Research Astronomers. Cambridge University Press, 2012. URL https://doi.org/10.1017/CBO9781139059503.

R. Artusi, P. Verderio, and E. Marubini. Bravais-pearson and spearman correlation coefficients: Meaning, test of hypothesis and confidence interval. *The International Journal of Biological Markers*, 17(2):148–151, 2002. URL https://doi.org/10.1177/172460080201700213.

J. L. Bertaux, R. Lallement, S. Ferron, C. Boonne, and R. Bodichon. Tapas, a web-based service of atmospheric transmission computation for astronomy. *Astronomy & Astrophysics*, 564:A46, 2014. URL http://dx.doi.org/10.1051/0004-6361/201322383.

D. L. Bones, J. D. Carrillo-Sánchez, A. N Kulak, and J. M. C. Plane. Ablation of Ni from micrometeoroids in the upper atmosphere: Experimental and computer simulations and implications for Fe ablation. *Planetary and Space Science*, 179:104725, 2019. URL https://doi.org/10.1016/j.pss.2019.104725.

J. Borovička. A fireball spectrum analysis. *Astronomy & Astrophysics*, 279(2):627–645, 1993. URL https://ui.adsabs.harvard.edu/abs/1993A&A...279..627B.

J. Borovička, R. Stork, and J. Bocek. First results from video spectroscopy of 1998 leonid meteors. *Meteoritics & Planetary Science*, 34(6):987–994, 1999. URL https://doi.org/10.1111/j.1945-5100.1999.tb01418.x.

J. Borovička, P. Koten, P. Spurný, J. Boček, and R. Štork. A survey of meteor spectra and orbits: evidence for three populations of Na-free meteoroids. *Icarus*, 174(1):15 – 30, 2005. URL https://doi.org/10.1016/j.icarus.2004.09.011.

A. Bounhir and Z. Benkhaldoun. Study of AERONET data of nearby stations in the Canary Islands: application to infer astronomical extinction coefficient at elevated altitudes. In Richard H. Picard, Klaus Schäfer, Adolfo Comeron, and Michiel van Weele, editors, *Remote Sensing of Clouds and the Atmosphere XV*, volume 7827, pages 204 – 218. International Society for Optics and Photonics, SPIE, 2010. URL https://doi.org/10.1117/12.866159.

C. Buil. How to calculate the spectral response of a spectrograph [online], 2019. URL http://www.astrosurf.com/buil/instrument_response_us/. Last visited: 02 May 2021.

L. R. Cander. *Ionospheric Space Weather*. Springer Nature Switzerland, 2019. URL https://www.springer.com/gp/book/9783319993300.

D. Cecil and M. Campbell-Brown. The Application of Convolutional Neural Networks to the Automation of a Meteor Detection Pipeline. *Planetary and Space Science*, 186:104920, 2020a. URL https://doi.org/10.1016/j.pss.2020.104920.

D. Cecil and M. Campbell-Brown. Data for: The Application of Convolutional Neural Networks to the Automation of a Meteor Detection Pipeline. *Mendeley Data, v1*, 2020b. URL https://doi.org/10.17632/g36g9rj3xj.1.

Z. Ceplecha, J. Borovička, W. G. Elford, D. O. ReVelle, R. L. Hawkes, V. Porubčan, and M. Šimek. Meteor Phenomena and Bodies. *Space Science Reviews*, 84:327–471, 1998. URL https://doi.org/10.1023/A:1005069928850.

M. De Cicco, S. Zoghbi, A. P. Stapper, A. J. Ordoñez, J. Collison, P. S. Gural, S. Ganju, J. L. Galache, and

P. Jenniskens. Artificial intelligence techniques for automating the CAMS processing pipeline to direct the search for long-period comets. In *Proceedings of the International Meteor Conference*, pages 65–70, January 2018. URL https://ui.adsabs.harvard.edu/abs/2018pimo.conf...65D.

M. Dubs and K. Maeda. Calibration of meteor spectra. In A. Roggemans and P. Roggemans, editors, *International Meteor Conference Egmond, the Netherlands, 2-5 June 2016*, page 65, 2016. URL https://ui.adsabs.harvard.edu/abs/2016pimo.conf...65D.

E. D. Feigelson and G. J. Babu. *Statistical Methods for Astronomy*, pages 445–480. Springer Netherlands, Dordrecht, 2013. URL https://doi.org/10.1007/978-94-007-5618-2_10.

D. Foreman-Mackey, D. W. Hogg, D. Lang, and J. Goodman. emcee: The MCMC Hammer. *Publications of the Astronomical Society of the Pacific*, 125(925):306, March 2013. URL https://doi.org/10.1086/670067.

Y. Galindo and A. C. Lorena. Deep Transfer Learning for Meteor Detection. In *Anais do XV Encontro Nacional de Inteligência Artificial e Computacional*, pages 528–537. SBC, 2018. URL https://doi.org/10.5753/eniac.2018.4445.

A. Gelman, J. B. Carlin, H. S. Stern, D. B. Dunson, A. Vehtari, and D. B. Rubin. *Bayesian Data Analysis (3rd ed.)*. Chapman and Hall/CRC, 2013. URL https://doi.org/10.1201/b16018.

J. Goodman and J. Weare. Ensemble samplers with affine invariance. *Communications in Applied Mathematics and Computational Science*, 5(1):65 – 80, 2010. URL https://doi.org/10.2140/camcos.2010.5.65.

M. Gritsevich and D. Koschny. Constraining the luminous efficiency of meteors. *Icarus*, 212(2):877 – 884, 2011. URL https://doi.org/10.1016/j.icarus.2011.01.033.

P. Jenniskens. Quantitative meteor spectroscopy: Elemental abundances. *Advances in Space Research*, 39(4):491 – 512, 2007. URL https://doi.org/10.1016/j.asr.2007.03.040.

Peter Jenniskens, Christophe Laux, Michael Wilson, and Emily Schaller. The mass and speed dependence of meteor air plasma temperatures. *Astrobiology*, 4: 81–94, 02 2004. URL https://doi.orf/10.1089/153110704773600258.

S. Jin, H. Ju, and H. Jung. Adaptive Markov chain Monte Carlo algorithms for Bayesian inference: recent advances and comparative study. *Structure and Infrastructure Engineering*, 15(11):1548–1565, 2019. URL https://doi.org/10.1080/15732479.2019.1628077.

D. Koschny and J. Borovicka. Definitions of terms in meteor astronomy. *WGN, Journal of the International Meteor Organization*, 45(5):91–92, October 2017. URL https://ui.adsabs.harvard.edu/abs/2017JIMO...45...91K.

D. Koschny and J. Diaz del Rio. Meteor Orbit and Trajectory Software (MOTS) - Determining the Position of a Meteor with Respect to the Earth Using Data Collected with the Software MetRec. *WGN, Journal of the International Meteor Organization*, 30(4):87–101, August 2002. URL https://ui.adsabs.harvard.edu/abs/2002JIMO...30...87K.

D. Koschny, F. Bettonvil, J. Licandro, C. v. d. Luijt, J. Mc Auliffe, H. Smit, H. Svedhem, F. de Wit, O. Witasse, and J. Zender. A double-station meteor camera set-up in the Canary Islands – CILBO. *Geoscientific Instrumentation, Methods and Data Systems*, 2(2): 339–348, 2013. URL https://doi.org/10.5194/gi-2-339-2013.

R. Landman. Bayesian inference of meteor spectra. Leiden Observatory, Leiden University Theses (M.Sc. thesis). Unpublished, 2020.

Heiko Liebhart, Markus Fertig, Georg Herdrich, Stefanos Fasoulas, and Hans-Peter Roser. Demonstration of the Capabilities of Parade with Regard to the Calculation of the Linear Tri-Atomic Molecule CO2. In *Radiation of High Temperature Gases in Atmospheric Entry*, volume 689 of *ESA Special Publication*, page 25, February 2011. URL https://ui.adsabs.harvard.edu/abs/2011ESASP.689E..25L.

E.G. Loewen and E. Popov. *Diffraction Gratings and Applications (1st ed.)*. CRC Press, 1997. URL https://doi.org//10.1201/9781315214849.

S. Löhle, F. Zander, T. Hermann, M. Eberhart, A. Meindl, R. Oefele, J. Vaubaillon, F. Colas, P. Vernazza, A. Drouard, and J. Gattacceca. Experimental simulation of meteorite ablation during earth entry using a plasma wind tunnel. *The Astrophysical Journal*, 837(2):112, 2017. URL https://doi.org/10.3847/1538-4357/aa5cb5.

P. Matlovič, J. Tóth, L. Kornoš, and L. Löhle. On the sodium enhancement in spectra of slow meteors and the origin of Na-rich meteoroids. *Icarus*, 347:113817, 2020. ISSN 0019-1035. URL https://doi.org/10.1016/j.icarus.2020.113817.

S. Molau. The meteor detection software MetRec. In W. J. Baggaley and V. Porubcan, editors, *Meteroids 1998*, page 131, jan 1999. URL https://ui.adsabs.harvard.edu/abs/1999md98.conf..131M.

L. Neslusan and M. Hajduková. Meteor showers of comet c/1964 n1 (ikeya). *Astronomy & Astrophysics*, 616:A162, 2018. URL https://doi.org/10.1051/0004-6361/201832829.

T. Ott, E. Drolshagen, D. Koschny, G. Drolshagen, and B. Poppe. Meteoroid flux determination using image intensified video camera data from the CILBO double station. In J. L. Rault and P. Roggemans, editors, *Proceedings of the International Meteor Conference, Giron, France, 18-21 September 2014*, pages 23–29, February 2014. URL https://ui.adsabs.harvard.edu/abs/2014pim4.conf...230.

S. Gopal Krishna Patro and K. Kumar Sahu. Normalization: A preprocessing stage. *IARJSET*, abs/1503.06462, 03 2015. URL https://www.doi.org/10.17148/IARJSET.2015.2305.

R. Rudawska, J. Zender, D. Koschny, H. Smit, S. Löhle, F. Zander, M. Eberhart, A. Meindl, and I. Uriarte Latorre. A spectroscopy pipeline for the canary island long baseline observatory meteor detection system. *Planetary and Space Science*, 180:104773, 2020. URL https://doi.org/10.1016/j.pss.2019.104773.

S. Sharma. Markov Chain Monte Carlo Methods for Bayesian Data Analysis in Astronomy. *Annual Review of Astronomy and Astrophysics*, 55(1): 213–259, 2017. URL https://doi.org/10.1146/annurev-astro-082214-122339.

E. A. Silber, M. Boslough, W. K. Hocking, M. Gritsevich, and R. W. Whitaker. Physics of meteor generated shock waves in the earth's atmosphere – a review. *Advances in Space Research*, 62(3):489 – 532, 2018. ISSN 0273-1177. URL https://doi.org/10.1016/j.asr.2018.05.010.

J. M. Trigo-Rodríguez, J. Llorca, and J. Fabregat. Chemical abundances determined from meteor spectra — II. Evidence for enlarged sodium abundances in meteoroids. *Monthly Notices of the Royal Astronomical Society*, 348(3):802–810, 03 2004. URL https://doi.org/10.1111/j.1365-2966.2004.07389.x.

J. Vaubaillon, P. Koten, A. Margonis, J. Tóth, R. Rudawska, M. Gritsevich, J. Zender, J. McAuliffe, P. D. Pautet, P. Jenniskens, D. Koschny, F. Colas, S. Bouley, L. Maquet, A. Leroy, J. Lecacheux, J. Borovička, J. Watanabe, and J. Oberst. The 2011 Draconids: The First European Airborne Meteor Observation Campaign. *Earth, Moon, and Planets*, 114:137–157, 2015. URL https://doi.org/10.1007/s11038-014-9455-5.

V. Vojácek, J. Borovička, P. Koten, P. Spurný, and R. Stork. Catalogue of representative meteor spectra. *Astronomy&Astrophysics*, 580:A67, 2015. URL https://doi.org/10.1051/0004-6361/201425047.

V. Vojácek, J. Borovička, P. Koten, P. Spurný, and R. Stork. Properties of small meteoroids studied by meteor video observations. *Astronomy&Astrophysics*, 621:A68, 2019. URL https://doi.org/10.1051/0004-6361/201833289.

M. W. Winter, B. Pfeiffer, M. Fertig, and M. Auweter-Kurtz. Extension of PARADE to CO2 Plasmas and Comparison with Experimental Data in High Spectral Resolution for Air and CO2 Species. In *Radiation of High Temperature Gases in Atmospheric Entry*, volume 629 of *ESA Special Publication*, page 11, November 2006. URL https://ui.adsabs.harvard.edu/abs/2006ESASP.629E..11W.

J. Zender, D. Koschny, and K. Ravensberg. Calibration of spectral video observations in the visual: theoretical overview of the ViDAS calibration pipeline. In M. Gyssens, P. Roggemans, and P. Zoladek, editors, *Proceedings of the International Meteor Conference, Poznan, Poland, 22-25 August 2013*, pages 126–129, 2014. URL https://ui.adsabs.harvard.edu/abs/2014pim3.conf..126Z.

Recommendations for Future Work

The research presented in this paper fulfilled its objective of improving the quality of meteoroid composition inference from meteor spectra; it did so by developing a pipeline for the elevation-dependent spectral calibration of meteor spectra and by constraining the influence that atmospheric extinction, meteoroid entry conditions and temporal evolution of meteoroids have on meteor spectral appearances. Nonetheless, the time limitation of this project did not allow to further investigate areas of progress identified during this study, which could bring additional benefit to the quality of the spectral analysis, calibration and meteor detection pipelines. Thus, these areas represent material for recommended future research in this field. Depending on the length of the research project, different recommendations for future work may apply.

In the case of a short-period project (from 2 to 3 months long), two possible improvements to the calibration and analysis pipelines are encouraged. A first improvement could be made to the atmospheric calibration pipeline; it is recommended to incorporate the contributions of ozone and water vapour absorption in the pipeline, and assess their significance in the extinction correction. The atmospheric calibration is currently based on the assumption that extinction is uniquely caused by scattering of gas molecules and aerosols. However, it is known that ozone and water vapour have among the largest influence on atmospheric extinction. As observed from fig. 14, these are also two causes of the differences with the extinction estimates obtained from TAPAS. Differently than the scattering of gas molecules, though, the contributions of ozone and water vapour on atmospheric extinction have large variability over time; thus, they are difficult to approximate through mathematical modelling. For this reason, readings from on-ground or space-borne instruments might be a more reliable means to quantify ozone and water vapour optical thicknesses in this future work.

The other area of improvement concerns the meteor spectral analysis. Specifically, future researchers are encouraged to add more elements to the set currently used in our pipeline (listed in table 4). In our research, the selection of the elements used for the modelling of synthetic meteor spectra was based on past findings by Borovička (1993), Borovička et al. (2005) and Jenniskens (2007). However, constraining the analysis only on elements which already appeared in past studies limits the possibility for new discoveries. Nevertheless, the set of elements to estimate should be enlarged with caution: estimating more elements may increase the computational time, as one may need more iterations of the MCMC to obtain equally accurate results. Also, the quality of results worsens if one tries to estimate the abundance of an element which in reality did not belong to the meteoroid; hence these additions should always have a theoretical or experimental rationale. Among the new elements to include within the spectral fitting pipeline, the addition of Ni is recommended — laboratory experiments by Bones et al. (2019) showed the significance of Ni emissions in the spectra of ablating meteorites and highlighted that knowledge about Ni excitation allows to better interpret Fe ablation.

In case of future theses or internships (more than 3 months long), a highly recommended work is to incorporate machine learning (ML) algorithms as part of the meteor detection pipeline. At the early stages of data reduction, meteor scientists are often faced with extremely large amount of data, which require lengthy manual filtering to remove false detections, e.g. satellites, camera noise and others. In our research project, for example, the process of selection of visible events (described in section 2.2) took around 3 weeks. The use of a ML automated process would reduce the burden on researchers, remove possible sources of human error and, if applied real-time, result in storage savings for CILBO computers. An interesting application of ML to meteor detection is discussed in Cecil and Campbell-Brown (2020a). Future work on this field can thus take inspiration from the convolutional neural network (CNN) algorithm described in this paper, which showed a notable success rate of 99.98% in filtering meteor samples. The data they used for the algorithm testing is accessible via Cecil and Campbell-Brown (2020b); this may prove useful as a first database for ML application in the MRG. Other successful implementations of CNN for meteor detection are described in De Cicco et al. (2018) and Galindo and Lorena (2018).

From our research, we concluded that there exists an uncertainty in the pixel position of the meteor's zeroth-order provided by MetRec[7]. In particular, it is still unclear whether MetRec provides information about the ICC8 pixel position of the zeroth-order for the meteor's highest point (meteor tail), lowest point (meteor nucleus) or brightest point. From the study presented in section 3.1.2, this uncertainty resulted to be a primary source of error in the wavelength calibration. Despite in this project we equipped the calibration pipeline with a procedure for wavelength error estimation (see appendix C), the research remains negatively affected by the presence of uncertainties in MetRec position estimates; the wavelength error estimation routine has substantial computational cost and its accuracy is dependent on the presence of dominant reference lines in the spectrum. Thus, a recommendation for future work is to improve the MetRec software, or implement a better performing one, for the purpose of reducing the uncertainty in the meteor position estimates. This would allow to reduce errors during wavelength calibration and ensure researches of higher quality and efficiency.

With the improvement of the calibration pipelines, new discoveries about the influence of external factors on meteoroids' composition inference and the automation of the processes, this study contributed to advance global

[7] MetRec is the software used within the MRG for meteor recognition

knowledge on meteor spectroscopy and boost future endeavours in this field at ESA and TU Deft. A logical continuation of this research in these institutes (long-term projects, longer than 7 months) could combine its results with dynamical analyses. In ESA, dynamical studies of meteors can be done using built-in tools for flux determination (Ott et al., 2014) and astrodynamic characterisation of meteoroids (Koschny and Diaz del Rio, 2002). Supported by and combined with our meteor spectroscopy analyses, the outcome of dynamical studies would allow to contribute to the research fields of meteor spectra classification and parent body associations, of great interest in today's meteor community. Linking to our study, dynamical research could, for example, relate the differences in the evolution along the meteor atmospheric trajectory (investigated in section 4.3.1) with the asteoroidal or cometary nature of the meteoroid's parent body; furthermore, it could clarify whether the yearly evolution of emissions from meteors belonging to the same shower (noted in section 4.3.2) is caused by the observation of different filaments of the meteoroid stream, or by different radiation exposures.

Meteor research within the MRG is directed towards the analysis of constantly bigger data sets, as CILBO cameras continue to be operative. Thanks to the automation of the calibration pipelines, ESA's MRG could now analyse larger sets of data in a reduced time. However, the computational cost of the MCMC Bayesian inference in the spectral analysis pipeline is still a great burden for time management. This is especially true if the analyses are performed on a regular personal PC, with limited performance capability: a Windows 10 laptop, 6 cores Intel i7 CPU at 2.60GHz could only analyse 1.1 event per hour. Future researchers would thus need to ensure their access, possibly also remote, to high-performance servers with a large number of CPUs over which to parallelise the computations. It is recommended to use more than 24 CPUs for the MCMC Bayesian inference. In fact, from our experience on Hipparchos, a 64-CPU Linux server managed within the Faculty of Aerospace Engineering at TU Delft and shared among more than 20 users, it takes around 170 h (~ 1 week) to analyse a set of 355 total meteor spectra using 24 CPUs.

Appendices

A. DATA REDUCTION: THE WEB INTERFACE

A web-based Graphical User Interface (GUI) was developed and used for the selection of meteor events to analyse within this project. An example of its layout is visualised in fig. A.0.1. The procedure for the selection of meteor spectra was composed of two steps: an automatic search of the events within CILBO's database, followed by a manual characterisation of the visible spectra among these events performed by the user.

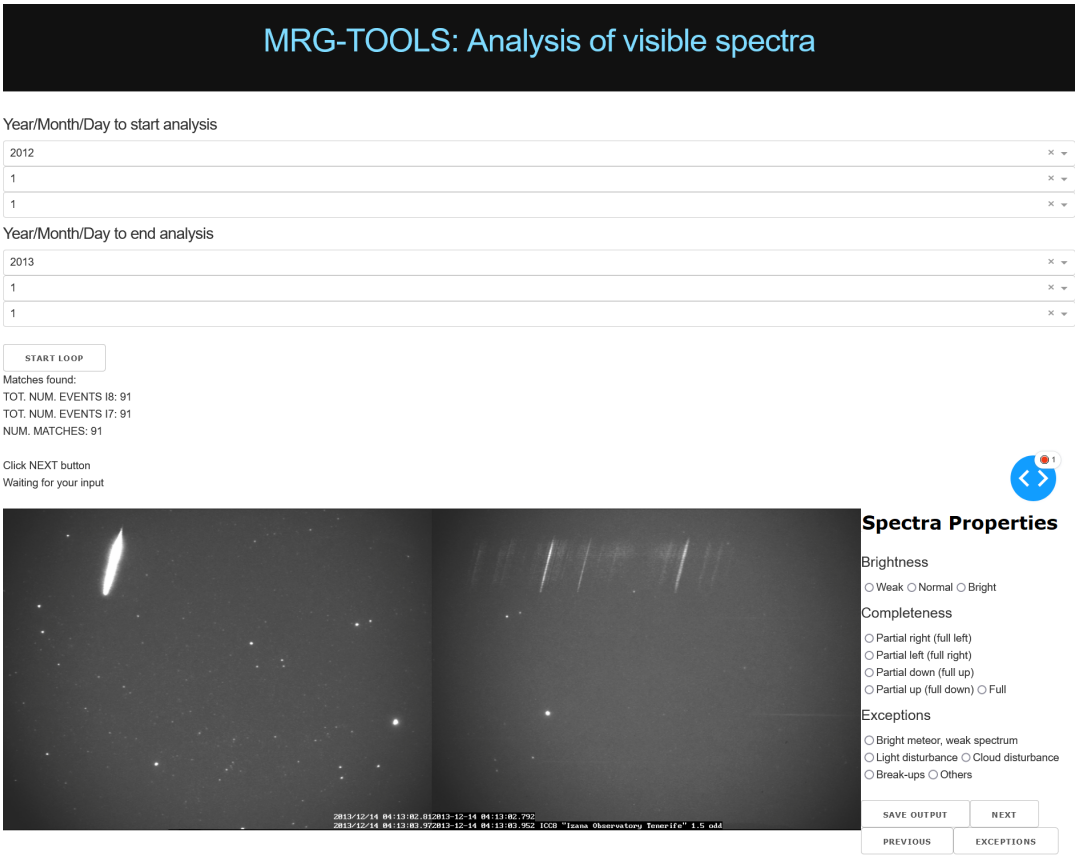

FIGURE A.0.1: Screenshot of the Graphical User Interface (GUI) developed for the selection of meteor spectra in this project. A bright, full event is shown in the images of this screenshot.

After running a dedicated Python script, the user is automatically directed to a web-page with the GUI. As a first step, the user is asked to insert the start date and end date of interest. Then, the "START LOOP" button is clicked. At this point, the script automatically searches for all meteor events available in ICC7 and ICC8 database for the dates of interest. The routine finds two sets with the number of events recorded by ICC7 and ICC8. Then, the number of matches between the two sets is found, as discussed in the last paragraph of section 2.2. Finally, the first match-event is displayed on screen: on the *left* the ICC7 zeroth-order meteor, on the *right* the ICC8 first-order spectrum. The use of the zeroth-order on the left allows to more easily identify the position of the meteor spectrum in the ICC8 image. This is especially useful for faint meteors. In fact, if considering that ICC8 has lower sensitivity than ICC7 due to the grating mounted on top, faint meteor events could be more easily identified on ICC7 images. The automatic search for matches takes an average of 5 s per observation year.

Following the automatic search of ICC7/ICC8 match events, these are manually characterised by the user. In particular, the user selects those events for which a first-order spectrum is visible within the ICC8 FOV. When a visible spectrum is spotted, this is characterised based on its brightness and completeness. Specifically, concerning the brightness, weak, normal and bright spectra are distinguished; regarding the completeness, partial and full spectra are separated, although for partial spectra a distinction is made based on which side of the spectrum is not fully within the ICC8 FOV at the time of observation. The spotted and characterised visible spectra are then collected in a database, after the user clicked "Save Output". In case that a match-event does not have a visible spectrum, the user clicks "Next", without characterising the event; the information of this event is collected into a separate database. Finally, in case of exceptional events, the user defines the type of exception seen and clicks "Exceptions" to save the output in a third different database. For the exceptional cases encountered, the spectrum was visible but the event was unusual; examples were bright meteors with faint spectra, cloud disturbance, light disturbance (e.g. Moon) and multiple break-ups in the atmosphere.

B. ASTROMETRY CALIBRATION

For the astrometric calibration, the external tool Astrometry.net was used. Astrometry.net is an open-access tool, available at https://nova.astrometry.net/. After users upload the images collected from their instruments, the tools performs the astrometric calibration: by recognising standard stars in the image uploaded, the tool estimates the celestial coordinates for each pixel of the image and generates a World Coordinate System (WCS). A WCS allows to correlate the pixel locations of a body on an image to its celestial coordinates, and vice versa. The ICC8 and ICC7 WCS used in this project were generated from the Astrometry.net calibration of the image collected by ICC8 and ICC7 on date 24/02/2012 03:38:25. The choice of the date to use was made considering the higher quality of these images.

Knowing that the observational set-up in CILBO was kept constant through the years, it was possible to use a unique WCS for both cameras to perform the astrometric calibration of all other dates as well. However, due to the Earth's rotation, the right ascension of the cameras' FOV would change per day. Thus, the angle estimated from the WCS needs to be corrected for the new right ascension at the moment of the observation. This can be easily done by using the sidereal time difference between the reference WCS and specific observation event; specifically, after taking the difference between the mean sidereal time of the Astrometry.net file with respect to the time of the observation considered, this difference is added to the reference right ascension of the astrofits file. The resulting WCS would then be expressed in the correct time frame and hence the astrometric calibration would be correct.

The accuracy of the astrometric calibration was verified using as reference the position on ICC7 and ICC8 frames of bright stars with known celestial coordinates — the WCS resulting from the astrometric calibration was used to map the star's known RA and Dec into the corresponding pixel locations (x, y) on ICC7 and ICC8 frames. The accuracy of the astrometric calibration was verified by the agreement between the calculated pixel locations and the reference position of the star visible on that frame. Figure B.0.1 shows the case of star Tania Borealis, as an example, where the calculated star's location (in *purple*) coincides with the reference position in both cameras (*white dot*).

This test was also used to check whether inaccuracies of astrometric calibration (errors in WCS) could be a possible cause of wavelength errors (section 3.1.2). At the end of this test, it was excluded the possibility that the wavelength calibration errors were due to inaccurate WCS generated during astrometric calibration.

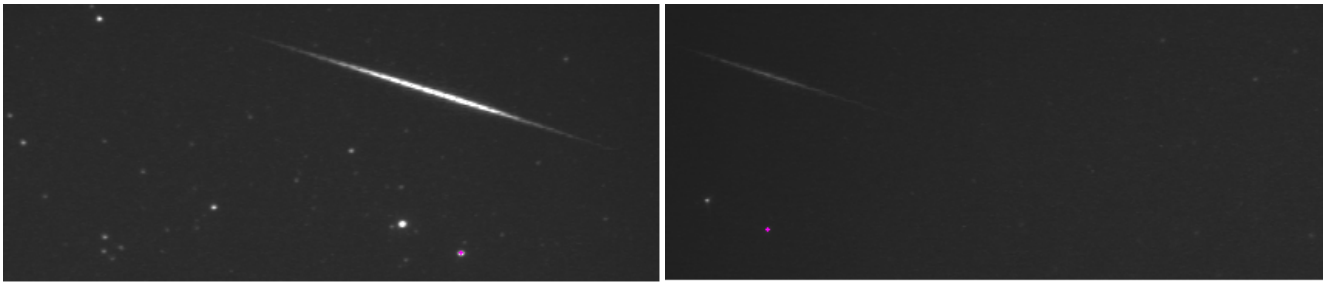

FIGURE B.0.1: Event 23/02/2012 03:38:24 — Tania Borealis location on ICC7 (*left*) and ICC8 (*right*). For both plots, the estimated star's location is represented with a purple dot; the reference star location is the white dot beneath the estimated one. In the ICC7 image, the reference star is partially visible beneath the purple dot, while on ICC8 this is completely covered by the purple dot; this is due to the lower sensitivity of ICC8 at the zeroth-order spectrum, making the zeroth-order star less visible (thus smaller) on ICC8 frames.

C. WAVELENGTH ERROR ESTIMATION

The algorithm of the Python routine developed in this project for the wavelength error estimation is presented in fig. C.0.1. This is based on the comparison between the wavelength associated to dominant features in the observed meteor spectrum and the wavelength position of reference atoms known from literature. The reference atoms used for the wavelength error estimation are Mg I (2), Na I (1) and O I (1), with wavelengths 518,2 nm, 589.2 nm and 777.4 nm, respectively (Borovička et al., 2005). The code is flexible: in case desired, the user could also decide to change the reference atoms used for the wavelength error estimation.

First, a dominant feature is searched within the observed meteor spectrum. In case its intensity dominates over the rest of the spectrum (case 1 in fig. C.0.1), this line is used for the wavelength error estimation; thus, the wavelength-position of this line is compared to the corresponding reference wavelength to estimate the error.

Differently (case 2), n_{lines} dominant lines are found around each neighbourhood ($\mathrm{wl}_{interval}$) of the three reference atoms; the wavelength distance of dominant lines to the reference line is calculated: overall, $3 \times n_{lines}$ different wavelength estimations are available. The search for n_{lines} dominant lines around the reference line takes into account that Mg, Na or O are not always the most intense lines in a spectrum. Due to the low resolution of video cameras, the number of spectral species which could be distinguished within an interval $\mathrm{wl}_{interval}$ is limited; hence, $n_{lines} = 3$ was used in this project. Wavelength errors are assumed constant over the entire meteor spectrum. Consequently, the wavelength error is the one for which the distance of local-dominant line to reference line is approximately equal for each of the three reference atoms above.

This method heavily relies on the presence of dominant lines in the observed spectrum, corresponding to reference emission lines — if Mg, Na or O lines are not dominant in the spectrum, the routine fails to estimate the wavelength error and associates an "Nan". Similarly, when the SNR is too low, it is difficult to spot a dominating line and the error estimation cannot be done accurately: thus, an "Nan" is provided instead of a numerical error estimation. Table C.1 gives a summary of the results from this wavelength error estimation routine.

Variable considered	*Value*
Years analysed	2012 to 2018
Total number of events analysed	355
Events with no error estimation	44 (12.4% of 355)
Events with an error estimation	311 (87.6% of 355)
Standard deviation (σ) of errors	6.547 nm
Arithmetic mean (μ) of errors	0.141 nm
Events with errors within $\pm 1\,\sigma$	80.3% (of 311)
Errors with errors within ± 10 nm	89.8% (of 311)

TABLE C.1: Statistics on the wavelength errors estimated via the wavelength calibration routine.

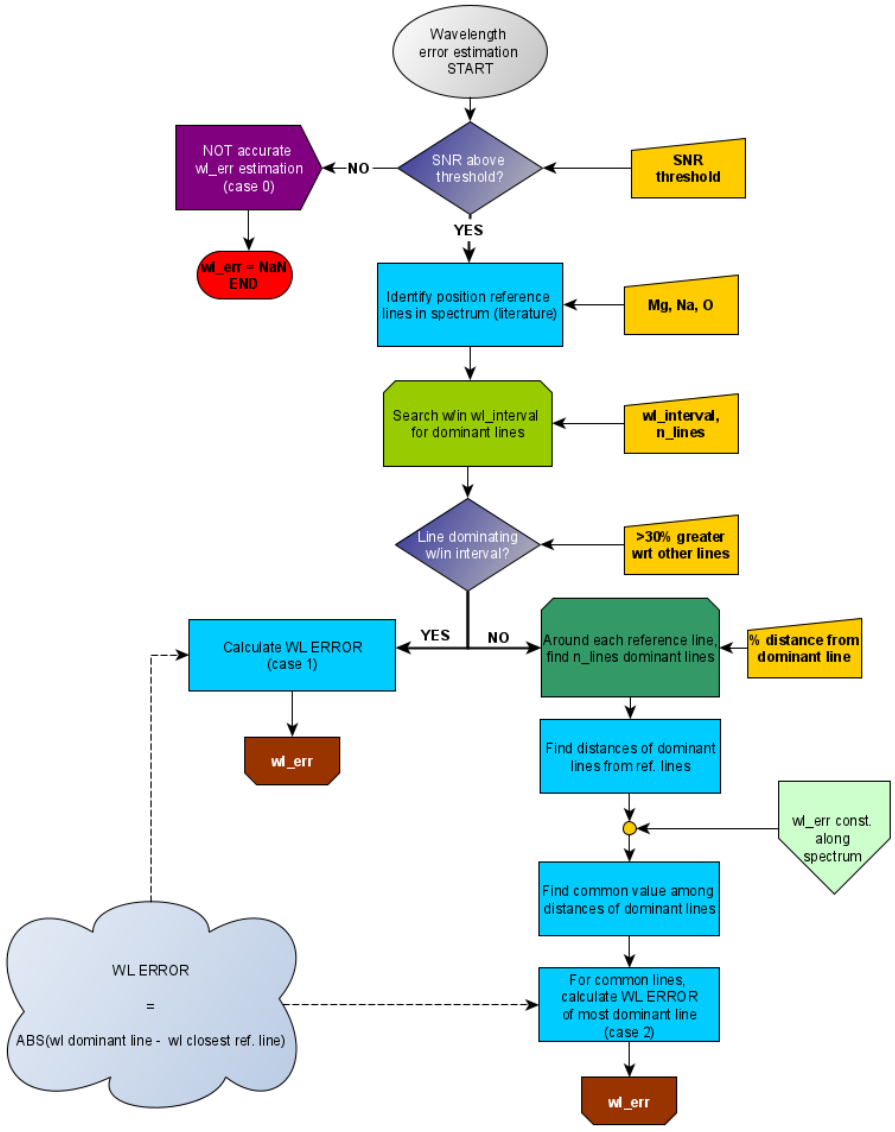

FIGURE C.0.1: Algorithm of the Python routine developed in this project to estimate the error in the wavelength calibration.

D. CORRECTION FOR UNCERTAINTIES IN METREC: ROW-INTEGRATION OF METEOR SPECTRA

To correct for the uncertainties in the Metrec information about the position of the zeroth-order meteor, which particularly affect the vertical positioning of the calibration box (section 3.1.3), the meteor spectra are integrated over multiple rows within the frame considered. The algorithm implemented is schematised in fig. D.0.1 and presented below:

1) The calibration box is estimated using the pipeline in section 3.1.1, with Metrec information as input. The box has horizontal side equal to the difference between the maximum and minimum location of the ICC8 first-order spectrum on the image's x-axis (x_λ in section 3.1.1, with λ being the wavelength); the box is vertically centred at the median value among the locations of the ICC8 first-order spectrum on the image's y-axis (y_λ) and has vertical side of 50 px.
2) A local search finds the position of the brightest row within the calibration box, i.e. the horizontal line for which the sum of all pixels' intensities within the box is greatest. This row is where the calibration box would be centred, in the absence of Metrec errors.
3) Having found the brightest row of the frame, the Δy could be estimated. The Δy represents the distance on the y-axis between the calibration box's brightest row and its actual centre; it shows how much the calibration box should be projected along the y-axis of the image for it to be centred at the brightest row.
4) The spectrum slope (s) is estimated by considering the x- and y-axis pixel locations of the same spectral feature (x_λ, y_λ) across two consecutive frames:

$$s = \frac{y_\lambda^{\text{frame 1}} - y_\lambda^{\text{frame 2}}}{x_\lambda^{\text{frame 1}} - x_\lambda^{\text{frame 2}}} \tag{D.0.1}$$

   Knowing s and Δy, the displacement along the x-axis could be estimated as defined below:

$$\Delta x = \frac{\Delta y}{s} \tag{D.0.2}$$

   Please note that this Δx is different from the wavelength error estimated in appendix C. The Δx shows the displacement along the x-axis needed to project the calibration box to the brightest row, with the projection being done along the meteor's trajectory. The meteor trajectory is generally not a straight line so the calibration box projection will have an x- and y-displacement term. Differently, the wavelength error estimated in appendix C represents the error resulting from the wavelength calibration procedure which affects the spectrum, even before its projection.
5) The calibration box is moved up and down depending on Δy, left and right depending on Δx. After the projection, the box is centred at the frame's brightest row.
6) Each feature of the spectral profile is computed by adding up, along the spectrum slope, the intensities of the pixels within the projected box.

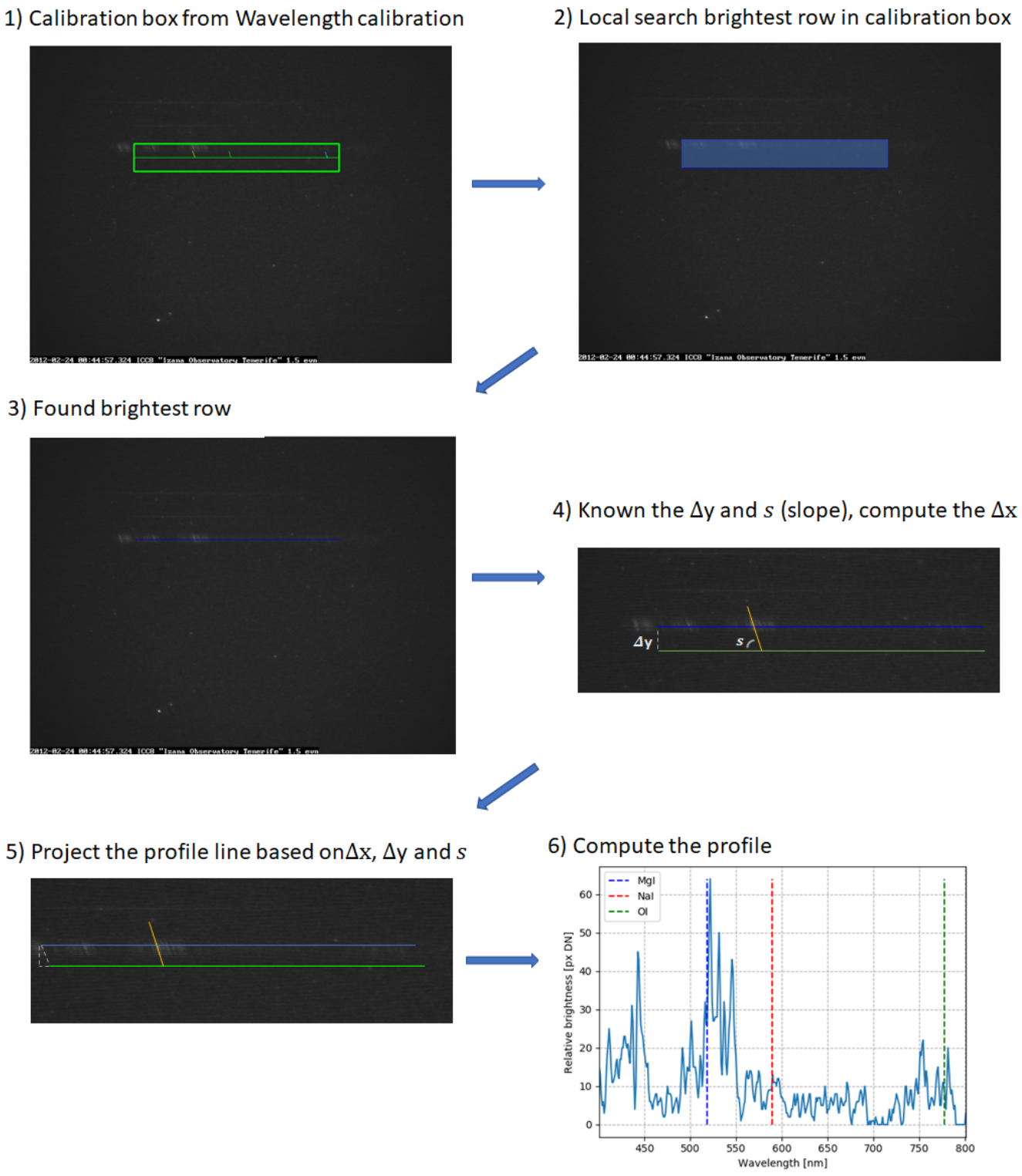

FIGURE D.0.1: Schematic of the method used to compute the profile: integration over multiple rows within the same frame.

E. ATMOSPHERIC CALIBRATION: THE AEROSOLS' CONTRIBUTION

To account for the Aerosol Optical Thickness, NASA's AERONET database was used. The database is found at https://aeronet.gsfc.nasa.gov/new_web/aerosols.html. The file which contained the data used was named "Aerosol Optical Depth (AOD) with Precipitable Water and Angstrom Parameter". The data downloaded were the daily average aerosol optical thickness as observed by an AERONET sun-photometer located in Izana, Spain (Tenerife). This AERONET station (longitude of 16.5° W, latitude of 28.3° N, altitude of 2367 m, according to Bounhir and Benkhaldoun (2010)) was extremely close to the CILBO-T station in Tenerife (longitude of 16.511° W, latitude of 28.301° N, altitude of 2395 m, according to Koschny et al. (2013)): around 1.17 km of ground distance between the two stations. In view of the proximity between the two stations, we assume that the aerosol optical thickness obtained from Izana to first order could be valid for our CILBO-T station as well.

The aerosol optical thickness values were provided at discrete, irregular intervals from 340 nm to 870 nm. The overall optical thickness ($\mathbf{b_{sca}}$ in eq. (8)) was obtained by combining the Rayleigh optical thickness of gas molecules (retrieved using eq. (10)) with the aerosol optical thickness values obtained from the AERONET database. To do so, the aerosol optical thickness was interpolated to the wavelengths of the Rayleigh optical thickness, spaced at half the spectral resolution of ICC8 camera (≈1 nm/px). This is the same interval at which gas molecules' optical thickness is provided.

F. MARKOV CHAIN MONTE CARLO SAMPLING

The parameters to estimate as part of the meteor spectral analysis (listed in table 3) are sampled following the Markov Chain Monte Carlo (MCMC) sampling method. This method generates parameters' samples around first-guess values, following a probability which is proportional to the posterior, i.e. the probability over the parameter provided the meteor spectral data. The sampling equation is reported below:

$$n\theta d\theta \propto P(\theta|Y)d\theta \tag{F.0.1}$$

with θ being the parameter value, $n(\theta)$ how many samples there are between values θ and $\theta + d\theta$, and $P(\theta|Y)$ the posterior.

Various MCMC samplers are available in literature and used for astronomy and engineering research, such as the Metropolis-Hastings sampler or the affine-invariance sampler. All of the MCMC samplers follow Markov property, from which the estimation of the next sample is only based on the most current sample value (Landman, 2020):

$$P(\theta_i|\theta_{i-1},...,\theta_{i-N}) = P(\theta_i|\theta_{i-1}) \tag{F.0.2}$$

Figure F.0.1 schematises how an MCMC sampling works. In this research, the affine-invariance sampler is used, which is freely accessible via the Python package *emcee* through the "EnsembleSampler" class. The choice of this sampler is advantageous in terms of computational time, as it allows to easily parallelise the sampling over multiple CPUs (Foreman-Mackey et al., 2013). Furthermore, this sampler allows to generate samples for a parameter without being affected by the co-variances with other parameters and without the need to manually tune the proposal distribution for all parameters (Goodman and Weare, 2010). The emcee sampler requires initialisation of the walkers; in this study, the initialisation is realised via a LSQ estimation, providing a first-guess parameter close to the maximum probability point.

The full description of this MCMC sampling is not within the scope of this paper. The interested reader is therefore highly encouraged to consult Goodman and Weare (2010) for more details about the affine-invariance sampler method and Foreman-Mackey et al. (2013) for a complete description of the installation and usage of the emcee Python package.

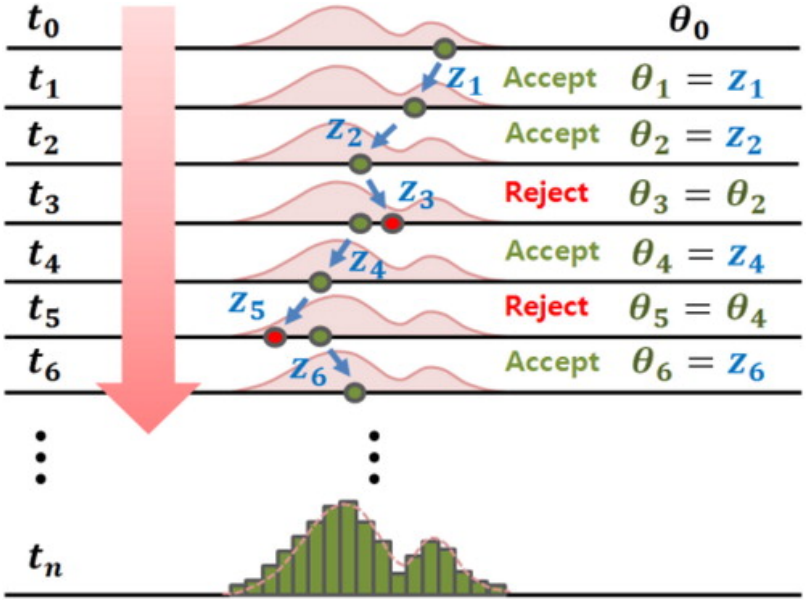

FIGURE F.0.1: Schematic of how an MCMC sampling algorithm works (Jin et al., 2019).

G. BAYESIAN INFERENCE OF METEOR SPECTRA

The inference of meteoroid composition from meteor spectra is performed in this project using Bayesian probability (Gelman et al., 2013). In particular, *Bayes' theorem* applied to our problem and in natural-logarithmic scale becomes:

$$\ln P(\theta|Y) = \ln L(Y|\theta) + \ln \pi(\theta) - \ln \pi(Y) \tag{G.0.1}$$

where $P(\theta|Y)$ is the *posterior*, i.e. the probability over the parameter provided the data, $L(Y|\theta)$ is the *likelihood*, i.e. the probability that the data occurs given the parameters, and $\pi(\theta)$ is the *prior*, i.e. the probability that the parameters occur. The term $\pi(Y)$, called *evidence*, would not be considered in our problem, as we used a Markov Chain Monte Carlo (MCMC) approach for the parameter estimation (Sharma, 2017).

In our case, the data (Y) are the spectral lines' intensities of the meteor spectra. The parameters (θ) are summarised in table 3. The scope of the Bayesian inference is to estimate the posterior. By applying a MCMC analysis, the best-fit estimate for all of the parameters considered is retrieved at the end of the meteor spectra analysis pipeline. The best-fit parameters represent those for which the posterior has highest value; specifically, the inference returns the combination of parameters for which the modelled (synthetic) spectra best fit the observed spectra (data).

As specified in Landman (2020), the priors represent what we already know about the parameters we aim to estimate. For their definition, different types of distributions were defined depending on the type of parameter considered:

- *Abundances (N), Gaussian broadening (σ) and temperatures (T)*: they were *all* considered as uniform priors. In a uniform distribution, all values have equal probability of occurrence; this means that the contribution $\pi(\theta)$ of these parameters in eq. (G.0.1) is a constant term, thus its logarithmic term $\ln \pi(\theta)$ is null.

- *Wavelength shift ($\Delta\lambda$)*: considered to follow a Gaussian distribution, expressed in eq. (G.0.2):

$$G(x) = \frac{1}{\sigma\sqrt{\pi}} \cdot \exp\left(-\frac{(x-\mu)^2}{2\sigma^2}\right) \tag{G.0.2}$$

  The natural-log of eq. (G.0.2), neglecting constant values, provides eq. (G.0.3), where μ is the expected value, i.e. the value obtained from the calculation of the wavelength error during the wavelength calibration (appendix C):

$$\ln \pi(\Delta\lambda) \propto -\frac{(\Delta\lambda - \mu)^2}{2} \tag{G.0.3}$$

- *Background (b)*: considered as a Jeffreys prior. The natural-log of this parameters' prior is expressed in eq. (G.0.4), where N represents the number of elements in the vector containing observed spectral data:

$$\begin{aligned} \pi(b) &= N\frac{1}{b} \\ \ln \pi(b) &= -N \ln b \end{aligned} \tag{G.0.4}$$

For the definition of the likelihood of the data, a Poisson distribution was used, according to the previous research conducted by Landman (2020):

$$\ln L(Y|\theta) = \sum_i y_i \ln\left(f(x_i|\theta)\right) - f(x_i|\theta) - \cancel{\ln(y_i!)} \tag{G.0.5}$$

where y_i is an item of the data vector Y (observed spectrum) and $f(x_i|\theta)$ is expression of the radiative transfer model used (x_i is an item of the synthetic spectrum). The last term of eq. (G.0.5) is cancelled, as it was not included in the formulation of the likelihood in the Python routine. In fact, as data does not change during the MCMC simulation, that term is constant and thus would not have influence in the relative studies performed on elemental abundances.

H. SELECTION OF EVENTS FOR INDIVIDUAL FRAMES' ANALYSIS

From a preliminary analysis of individual frames' spectra, it was observed that, for a considerable set of events, the UV part of the spectrum appears at lower heights than the rest of of elements emitted in the visible spectrum. With lower heights, the atmospheric pressure increases and so does the ablation temperature, while the atmospheric extinction decreases. Both increased temperature and decreased extinction with lower height could be the cause of the observed later emission of UV features. However, these are causes of different nature: the former would be linked to the ablation conditions, while the latter to the atmosphere and hence could be solved if performing an altitude-dependent correction for the atmosphere.

To study these effects, the analysis was performed on a set of the events for which an increase of UV features towards heights was observed. Before applying the routine for meteor spectral analysis described in section 4.1.1, the events for which to study the individual frames were selected. Meteors belonging to meteor showers were preferred, as their parent bodies had similar history in space, composition and structure. Consequently, they should present similar parent compositions, thus any change with height could be more easily interpreted.

Meteors generated from five meteor showers were selected, for which the number of events available over the different years of observation was significant. Among those: ANT (Radiant of Antihelion) had the greatest amount of cases, PER and GEM (Perseids and Geminids) had more literature sources which could be used for reference, STA and ORI (Southern Taurids and Orionids) had a good amount of data, though no altitude information for the events associated. However, the UV increase with height was not observed in all of these events; hence a case-by-case selection was applied. This resulted in a selection of 26 events, for a total of frames 680 frames, of which 373 with SNR above 2.3 (those were the ones analysed via Bayesian Inference). The events belonged to the five showers listed above, which appear bold in table H.1.

The events selected will then be used for the analysis of elements' emission along the meteor's path in section 4.3.1, done using spectra of individual frames. By contrast, section 4.3.2 of the draft paper only presented results from ANT and GEM meteors, since they were the most interesting ones for that analysis on the time evolution of shower meteor's emissions.

Shower	*Year*							*Height*
	2012	*2013*	*2014*	*2015*	*2016*	*2017*	*2018*	
ANT (Radiant of Antihelion)	**12**	**9**	**5**	**5**	**5**	**-**	**-**	**100.94 - 83.67**
CAP (α-Capricornids)	-	-	2	-	1	-	-	90.81 (1 case)
COM (Coma Berenicids)	-	-	1	-	-	1	-	N/A
DAU (δ-Aurigids)	-	-	-	-	1	-	-	N/A
DLE (δ–Leonids)	-	-	1	-	-	-	-	N/A
DSX (Daytime Sextantids)	-	-	-	-	1	-	-	N/A
EGE (ϵ-Geminids)	-	1	-	-	-	-	-	109.77 (1 case)
ETA (η-Aquarids)	3	1	-	-	-	-	-	106.07 - 99.58
GEM (Geminids)	**-**	**12**	**-**	**7**	**1**	**4**	**-**	**92.03 - 87.02**
JBO (June Bootids)	-	1	-	-	-	-	-	N/A
LMI (Leonis Minorids)	-	1	-	-	-	-	-	N/A
LYR (Lyrids)	1	-	-	-	-	-	-	98.65 (1 case)
MON (Northern Taurids)	-	-	-	-	2	-	-	N/A
NTA (Northern Taurids)	2	3	-	-	2	-	-	N/A
ORI (Orionids)	**2**	**3**	**-**	**-**	**3**	**1**	**-**	**N/A**
PAU (Piscis Austrinids)	-	-	-	-	1	-	-	N/A
PER (Perseids)	**-**	**4**	**1**	**6**	**3**	**-**	**-**	**105.69 - 102.69**
PUP (Puppid/Velids)	-	-	-	1	-	-	-	N/A
QUA (Quadrantids)	-	-	1	-	1	-	-	N/A
SDA (South. δ-Aquarids)	-	2	-	-	2	-	-	91.74 (1 case)
SPE (September ϵ-Perseids)	1	-	-	-	1	-	-	N/A
SPO (Sporadics)	61	69	28	35	22	6	1	111.22 - 57.85
STA (Southern Taurids)	**7**	**4**	**-**	**-**	**2**	**-**	**-**	**N/A**
TUM (θ-Ursae Majorids)	2	-	-	-	-	-	-	N/A
OVERALL	*91*	*110*	*39*	*54*	*48*	*12*	*1*	*111.22-57.85*

TABLE H.1: Number of shower meteors and sporadics which are visible each year, considering the entire set of 355 visible events selected during data reduction (section 2.2). Last column indicates the height range. N/A are cases when the height estimation is not available. Bold showers are those selected for individual frames' analysis.